
SPAR: Self-supervised Placement-Aware Representation Learning for Multi-Node IoT Systems

Yizhuo Chen^{*1} Tianchen Wang^{*1} You Lyu¹ Yanlan Hu²
 Jinyang Li¹ Tomoyoshi Kimura¹ Hongjue Zhao¹ Yigong Hu¹
 Denizhan Kara¹ Tarek Abdelzaher¹

^{*}Equal Contribution ¹University of Illinois Urbana-Champaign

²Stanford University

Abstract

This work develops the underpinnings of self-supervised *placement-aware representation learning* given spatially-distributed (multi-view and multimodal) sensor observations, motivated by the need to represent external environmental state in multi-sensor IoT systems in a manner that correctly distills spatial phenomena from the distributed multi-vantage observations. The objective of sensing in IoT systems is, in general, to collectively represent an externally observed environment given multiple vantage points from which sensory observations occur. Pretraining of models that help interpret sensor data must therefore encode the relation between signals observed by sensors and the observers' vantage points in order to attain a representation that encodes the observed spatial phenomena in a manner informed by the specific placement of the measuring instruments, while allowing arbitrary placement. The work significantly advances self-supervised model pretraining from IoT signals beyond current solutions that often overlook the distinctive spatial nature of IoT data. Our framework explicitly learns the dependencies between measurements and geometric observer layouts and structural characteristics, guided by a core design principle: the duality between signals and observer positions. We further provide theoretical analyses from the perspectives of information theory and occlusion-invariant representation learning to offer insight into the rationale behind our design. Experiments on three real-world datasets—covering vehicle monitoring, human activity recognition, and earthquake localization—demonstrate the superior generalizability and robustness of our method across diverse modalities, sensor placements, application-level inference tasks, and spatial scales.

1 Introduction

The paper advances the state of the art in self-supervised *placement-aware representation learning*, motivated by Internet of Things (IoT) applications where multiple sensors of possibly different modalities and placement must collectively represent the state of their external environment. For example, a set of seismic and acoustic sensors placed around a critical choke point in a border defense application might collectively need to reconstruct the locations and types of potential intruders (e.g., humans, vehicles, stray animals) attempting to cross that choke point [34]. Alternatively, a set of accelerometers and gyroscopes placed on the human body might aim to collectively reconstruct the human activity performed [21]. In both examples, multimodal sensors of *different placement* observe the state of the target environment from different vantage points. An application aims to reconstruct the environmental state in a manner informed by sensor placement.

Sensor placement determines two important attributes of a sensor's vantage point or *position*; namely, *spatial location* and *structural information*. In the intruder detection scenario, spatial locations (such

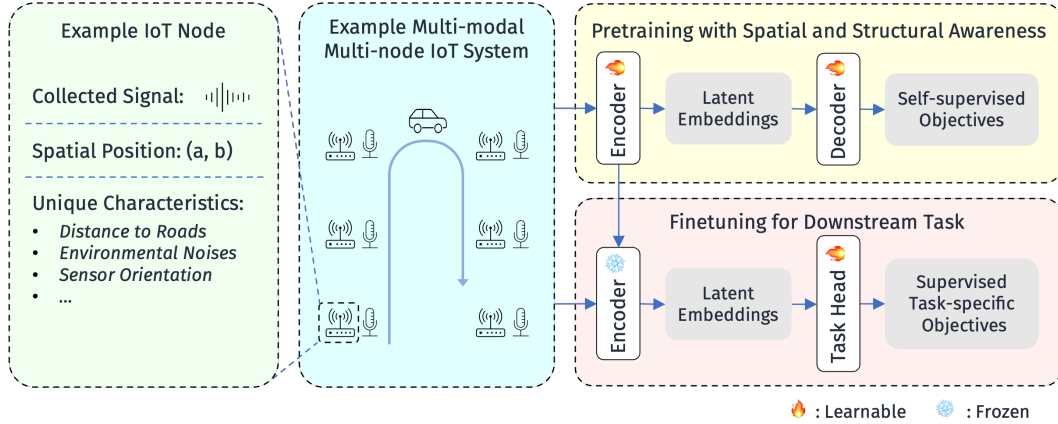


Figure 1: An overview of the SPAR workflow applied to a multi-modal multi-node IoT system. Each node from each modality collects its own signal and is associated with a spatial position, as well as unique characteristics that influence its signal patterns. During pretraining, SPAR encodes information from all these aspects to generate latent embeddings, optimized via self-supervised objectives on unlabeled data. In the fine-tuning stage, the encoder is frozen and used to extract representations, which are then fed into task-specific heads trained with labeled data for downstream tasks.

as GPS locations of sensors) dictate what part of the environment the sensor sees. In the human activity recognition scenario, structural information can indicate, for example, what part of the body the sensor is placed on (e.g., wrist-worn, head-mounted, etc). For a general framework, both location and structural information are important, although specific applications may focus on one or the other. We thus collectively refer to structural and location information as attributes of sensor *position*.

The work is motivated by the proliferation of *intelligent* IoT systems across domains ranging from smart cities [57] to autonomous vehicles [3], and from human activity recognition [26] to environmental sensing [61], amplifying the demand for generalizable and efficient learning frameworks that can represent the spatial environment robustly in the face of sensor placement variations. Pretraining has emerged as a promising approach to meet this need, especially under constraints like scarce labeled data and distribution shifts in downstream tasks [2, 4]. Recent IoT pretraining methods have achieved notable success by leveraging contrastive learning [50], masked reconstruction [28], and language-model-integrated designs [49]. While these approaches demonstrate strong performance within their respective settings, they often overlook a defining property of IoT data: its *multi-modal, multi-node structure embedded in physical space*. Unlike images [23] or text [42], IoT observations are tightly coupled with the spatial layout of sensor nodes and their structural metadata. These factors play a crucial role in shaping the observed signals, motivating solutions that interpret measured signals correctly given observer placement information.

Our method, SPAR, short for Self-supervised Placement-Aware Representation learning, is built on a central design philosophy: the *duality between positions and signals*. This principle recognizes that spatial and structural configurations are not auxiliary metadata but fundamental components of how signals are generated, propagated, and interpreted. Guided by this principle, our approach introduces three key components: (1) **spatial positional embeddings**, which encode the geometric location of sensing nodes, (2) **structural positional embeddings**, which capture other characteristics that influence signal behavior, and (3) **dual reconstruction objectives**, which enforce the mutual recoverability of signals and spatial positions with context awareness. Together, these components form a cohesive pretraining strategy that is both expressive and tailored to the intrinsic nature of IoT systems. An overview of the SPAR workflow is illustrated in Figure 1. While conceptually related efforts in the vision domain, such as NeRF and Gaussian Splatting [44, 29, 65], also leverage multi-view observations and spatial context, their goals differ fundamentally from ours. These methods aim to synthesize novel high-fidelity visual scenes. In contrast, SPAR is designed to learn informative context-aware representations for downstream inference tasks in IoT systems.

We conduct theoretical analyses from both information theory and occlusion-invariant representation learning [31] perspectives to uncover the insights and rationale behind our design. We further validate SPAR on three real-world datasets across diverse modalities and spatial configurations,

spanning applications of vehicle monitoring [34], human activity recognition [58], and earthquake localization [5], demonstrating consistent performance gains over existing methods.

To summarize, this paper makes the following key contributions: (1) We introduce SPAR, a novel IoT pretraining framework that explicitly models spatial layouts and node-specific characteristics, guided by the duality between positions and signals. (2) We provide theoretical analyses from information theory and occlusion-invariant representation learning to offer insight into the effectiveness of our design. (3) We conduct extensive experiments on three real-world datasets across diverse IoT scenarios to demonstrate SPAR’s generalizability and robustness.

2 Related Work

Pretraining and Foundation Models for IoT. Pretraining methods for IoT aim to learn generalizable representations from unlabeled data, enabling scalable and transferable learning across sensing tasks. Existing approaches largely fall into three paradigms: contrastive learning, generative (masked reconstruction) learning, and LLM-based frameworks. Contrastive learning methods primarily leverage the multi-modal nature of IoT data by aligning their embeddings in a shared representation space. Early works such as Cosmo [48], Cocoa [11], and FOCAL [41] focus on intra-sample contrast via modality-specific augmentations and projections. More recent models like ImageBind [17] and MMBind [50] extend this to loosely paired or unpaired modalities. Generative approaches rely on masked signal reconstruction [64, 10]. Ti-MAE [37], MOMENT [19], and TS-MAE [40] adapt masked autoencoding to time-series data, with TS-MAE incorporating a continuous-time formulation via differential equations. Other methods, such as FreqMAE [28] and PhyMask [27], explore frequency-domain masking and reconstruction objectives tailored to IoT signals. LLM-based frameworks aim to integrate sensor data into language-centric reasoning systems [20, 16]. LIMUBERT [69] adapts masked language modeling for inertial data, while recent works like Penetrative AI [68], LLMSense [49], and IoT-LM [45] introduce prompting strategies, summarization pipelines, and modality-specific adapters to enable cross-task transfer and zero-shot inference. While these approaches have shown strong empirical performance, they do not explicitly account for the spatial layout and node-specific characteristics that are fundamental to multi-node IoT systems. In contrast, our method incorporates spatial and structural information directly into the pretraining process, enhancing contextual grounding and robustness.

Pretraining with Different Notions of "Spatial" Context. Several pretraining approaches have sought to incorporate spatial context, though their definitions of "spatial" often differ from ours. In the visual domain, "spatial" may refer to grids of pixels or patches, as seen in works on video [14, 66], remote sensing [38, 52, 25], and 3D medical imaging [22]. Beyond visual data, many works use the term "spatial" to describe discrete symbolic entities in the data—commonly in the context of entity-wise masking strategies or the use of topological information, such as the joints in SkeletonMAE [67], the EEG channels in MV-SSTMA [35] and MMM [70], or sensor identities in Gao *et al.* [15] and Miao *et al.* [43]. In contrast, our approach integrates continuous physical coordinates of nodes explicitly into the pretraining pipeline, supporting more general modeling of spatial layouts that depart from linear token series or regular (patch/pixel) grids, accommodating arbitrary sensor placement topologies that sample the environment, and allowing generalization to unseen spatial configurations. Another conceptually related, but fundamentally different, direction is scene reconstruction and novel view synthesis in the vision domain [44, 29, 65], which similarly leverages spatial layouts and multi-view observations. However, these methods are typically optimized for synthesis quality and visual fidelity, differing from our goal of learning informative and transferable representations for IoT tasks.

Pretraining via Positional Reconstruction Objectives. Another line of work, though not designed for IoT data and often without explicitly using the term "spatial," incorporates various forms of positional reconstruction objectives in pretraining. In computer vision, Doersch *et al.* [12] proposed predicting relative patch positions, which was extended by Noroozi and Favaro [47] and Kim *et al.* [30] through jigsaw puzzle solving and content restoration tasks. DeepPermNet [53] learns permutation structures via differentiable sorting. MP3 [71] explores inferring absolute patch locations, while LOCA [7] predicts relative positions of clustered patches. In NLP, methods like StructBERT [63], ALBERT [32], and SLM [33] incorporate sentence order prediction and sequence restoration to model discourse structure, and recent work by Nandy *et al.* [46] further explores permutation-based objectives to capture procedural dependencies. Beyond vision and language, GeoMAE [59]

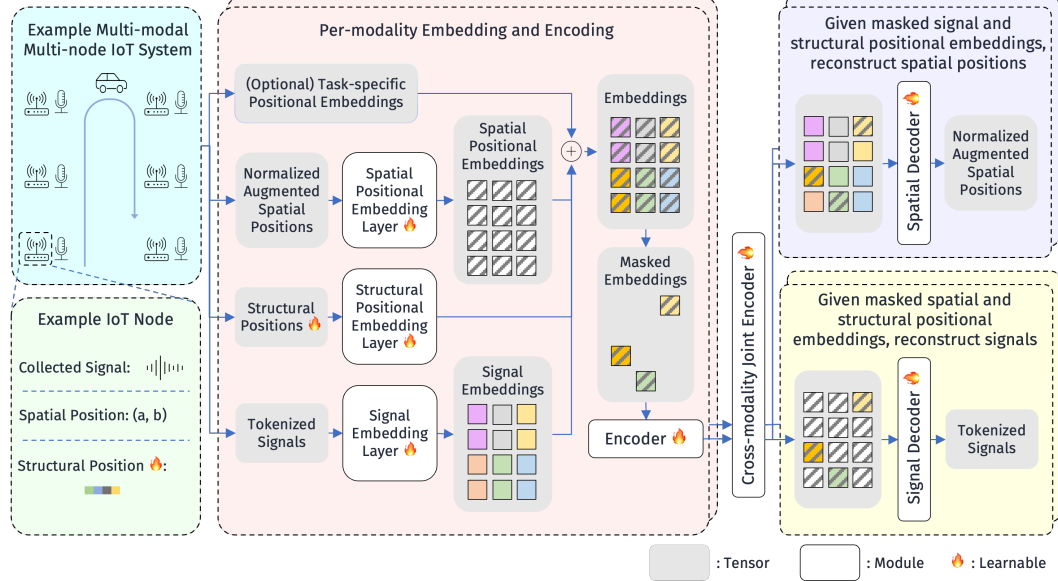


Figure 2: Architectural overview of SPAR. Each node is assigned a continuous learnable structural position to capture its unique characteristics. The signals, spatial positions, and structural positions of all nodes are projected into a shared embedding space, combined, and encoded into latent embeddings. The latent embeddings are optimized with dual reconstruction objectives, encouraging the model to effectively utilize and retain both signal and positional information in a self-supervised and context-aware manner.

reconstructs geometric features from masked point clouds, and LEGO [56] recovers perturbed molecular geometries to capture spatial arrangement at atomic resolution. While conceptually related to our work in leveraging positional reconstruction, these methods typically operate on discrete, domain-specific positional targets (e.g., patch indices or sentence order). By contrast, our method reconstructs continuous-valued physical positions of sensor nodes, which is more naturally suited to multi-node IoT systems.

3 Method

To develop a pretraining method that effectively utilizes the unique placement characteristics of IoT nodes, we propose SPAR, which explicitly leverages **the duality between observer placement and signals** in the IoT data. Specifically, we extend the traditional MAE framework by introducing **spatial positional embeddings** to represent device locations, and **structural positional embeddings** to encapsulate effects of other placement characteristics (such as orientation). Furthermore, we propose to optimize our model with novel **dual reconstruction objectives** to enhance its ability to retain both signal and spatial information in its learned representations. The overall architecture of SPAR is shown in Figure 2, with each component detailed below. Importantly, SPAR is grounded in solid theoretical foundations from both information theory and the study of occlusion-invariant representations, offering deep insights into our design.

For clarity, we adopt the following notation convention throughout the paper: scalars are denoted by lowercase or uppercase letters (e.g., k, K), matrices by bold uppercase letters (e.g., \mathbf{R}, \mathbf{S}), tensors by bold calligraphic letters (e.g., \mathcal{R}, \mathcal{S}), and random tensor variables by sans-serif uppercase letters (e.g., \mathbf{R}, \mathbf{S}). We use \mathcal{F} with appropriate subscripts to denote the forward operations of various transformer-based modules. A summary of notations is provided in Table 4 in Appendix A.

3.1 Embedding for Signals, Spatial Positions, and Structural Positions

We consider a multi-modality IoT sensing system with K modalities, where the k -th modality ($k \in \{1, \dots, K\}$) consists of $n^{(k)}$ sensing nodes. The signals collected from these nodes are first tokenized to be compatible with transformer encoders. The tokenization strategy is task-specific and flexible—for example, IMU time-series data can be divided into temporal segments, while acoustic spectrograms can be split into patches. We denote the tokenized signals as $\mathcal{X}^{(k)} \in \mathbb{R}^{n^{(k)} \times m^{(k)} \times d_{\mathcal{X}}^{(k)}}$,

where $m^{(k)}$ is the number of tokens and $d_{\mathcal{X}}^{(k)}$ is the token dimension. We then project these tokens into the transformer embedding space using a learnable linear layer, as $\tilde{\mathcal{X}}_{i,j,:}^{(k)} = \mathcal{F}_{\text{sig_embed}}^{(k)}(\mathcal{X}_{i,j,:}^{(k)})$, yielding signal embeddings $\tilde{\mathcal{X}}^{(k)} \in \mathbb{R}^{n^{(k)} \times m^{(k)} \times d}$, where d is the transformer model dimension.

A distinguishing aspect of IoT systems is the availability of **spatial positions** of the nodes, reflecting their physical layout in the field, which can be denoted as $\mathcal{S}^{(k)} \in \mathbb{R}^{n^{(k)} \times d_S}$. For instance, in Figure 2, the spatial positions are two-dimensional, indicating longitudinal and lateral node locations. Unlike the discrete ordinal indices typically used in NLP [62] or CV [13], spatial positions in IoT systems are continuous vectors, making classical positional embedding strategies unsuitable [62, 13, 55, 51]. To address this, we propose to continuously project the spatial positions into the embedding space as $\tilde{\mathcal{S}}_{i,j,:}^{(k)} = \mathcal{F}_{\text{sp_embed}}^{(k)}(\mathcal{S}_{i,j,:}^{(k)})$, where $\mathcal{S}_{i,j,:}^{(k)} = \mathcal{S}^{(k)}$ is the spatial positions broadcasted to match the dimension of the tokenized signals. The spatial positional embeddings $\tilde{\mathcal{S}}^{(k)}$ are then added to the signal embeddings to incorporate spatial context into the model.

However, two challenges arise in practice. First, spatial positions may vary widely in absolute locations and scales. For the example in Figure 2, data may be collected in different cities, with some layouts covering small parking lots and others spanning large open areas. To ensure consistency, we **normalize** the spatial positions of each sample to have zero mean and unit variance. Second, IoT datasets often contain only a limited number of distinct spatial layouts for which data were collected, leading the spatial embeddings (and the model) to overfit in pretraining, reducing generalizability to potentially unseen spatial arrangements during fine-tuning or testing. To mitigate this, we apply **geometric augmentation** during pretraining by randomly rotating and translating the normalized spatial positions, improving robustness to unseen layouts.

While spatial positions capture physical layout, they do not fully represent structural placement conditions, such as the body part a sensor is attached to, or the orientation used for a directional measurement device (e.g., front-facing versus rear-facing camera on an autonomous car). Manually labeling these characteristics for all nodes is often costly and non-scalable. To address this, we assign each node a continuous learnable vector, called **structural position**. The structural positions for all nodes are denoted as $\mathcal{R}^{(k)} \in \mathbb{R}^{n^{(k)} \times d_R}$, where we typically choose the dimension of structural position $d_R \ll d$ to ensure training efficiency and scalability to large-scale IoT systems. As with spatial positions, we broadcast $\mathcal{R}^{(k)}$ to form $\mathcal{R}^{(k)} \in \mathbb{R}^{n^{(k)} \times m^{(k)} \times d_R^{(k)}}$, project it into the embedding space via $\tilde{\mathcal{R}}_{i,j,:}^{(k)} = \mathcal{F}_{\text{st_embed}}^{(k)}(\mathcal{R}_{i,j,:}^{(k)})$, and add it to the signal embeddings. These learnable structural positions are trained jointly with the rest of the model in the pretraining stage, enabling it to automatically capture node-specific information.

Structural positions bear an interesting mathematical interpretation: if we assume the influence of a node’s unique characteristics on its signal embedding can be summarized as an additive vector, which lies within a specific subspace of the embedding space, then the weight matrix of $\mathcal{F}_{\text{st_embed}}^{(k)}$ can be understood as a learned set of basis vectors spanning this subspace. The structural position of each node can then be viewed as the coordinate of the corresponding additive vector in this subspace, thereby substantiating its meaning as an abstract “position”.

3.2 Masked Autoencoding with Dual Reconstruction Objectives

After combining the signal embeddings $\tilde{\mathcal{X}}^{(k)}$, spatial positional embeddings $\tilde{\mathcal{S}}^{(k)}$, and structural positional embeddings $\tilde{\mathcal{R}}^{(k)}$ (as well as any additional task-specific positional embeddings, such as 2D patch positions in a spectrogram, which we omit in the rest of this paper for clarity), we apply a binary mask $\mathcal{M}^{(k)} \in \{0, 1\}^{n^{(k)} \times m^{(k)}}$ over the combined embeddings to randomly mask out a fraction of tokens. The unmasked tokens are then fed into a per-modality transformer encoder to produce latent embeddings $\mathcal{Z}^{(k)}$:

$$\mathcal{Z}^{(k)} = \mathcal{F}_{\text{enc}}^{(k)}(\text{mask}(\tilde{\mathcal{X}}^{(k)} + \tilde{\mathcal{S}}^{(k)} + \tilde{\mathcal{R}}^{(k)}; \mathcal{M}^{(k)})), \quad (1)$$

where $\text{mask}(\cdot; \cdot)$ denotes the masking operation. To enable cross-modal interactions, we then apply a joint transformer encoder over the concatenated latent embeddings from all modalities:

$$(\tilde{\mathcal{Z}}^{(1)}, \dots, \tilde{\mathcal{Z}}^{(K)}) = \mathcal{F}_{\text{joint_enc}}(\text{concat}(\mathcal{Z}^{(1)}, \dots, \mathcal{Z}^{(K)})), \quad (2)$$

where $\text{concat}(\cdot)$ denotes concatenation, and $\tilde{\mathbf{Z}}^{(k)}$ denotes the post-fusion latent embeddings for the k -th modality. In the fine-tuning stage, the encoders are frozen, and the post-fusion latent embeddings are extracted and passed into a task-specific prediction head, which is trained using appropriate supervised objectives.

During the pretraining stage, however, the post-fusion latent embeddings are decoded, enabling the encoders to be optimized with self-supervised objectives. In the standard MAE framework, a single decoder is typically used to reconstruct the masked signals, which overlooks the rich spatial and structural context inherent in multi-node IoT data. To address this, we introduce two decoders with **dual reconstruction objectives**, explicitly exploiting the duality between positions and signals. Specifically, the **signal decoder** is tasked with reconstructing the masked signals, using both the latent embeddings and the masked spatial and structural positional embeddings:

$$\hat{\mathbf{x}}^{(k)} = \mathcal{F}_{\text{sig_dec}}^{(k)}(\text{concat}(\tilde{\mathbf{Z}}^{(k)}, \text{mask}(\tilde{\mathbf{S}}^{(k)} + \tilde{\mathbf{R}}^{(k)}; \overline{\mathbf{M}}^{(k)}))), \quad (3)$$

where $\overline{\mathbf{M}}^{(k)} = 1 - \mathbf{M}^{(k)}$ is the complement mask, and $\hat{\mathbf{x}}^{(k)}$ denotes the reconstructed signals. In parallel, the **spatial decoder** is responsible for reconstructing the masked spatial positions, conditioned on the latent embeddings and the masked signal and structural positional embeddings:

$$\hat{\mathbf{S}}^{(k)} = \mathcal{F}_{\text{sp_dec}}^{(k)}(\text{concat}(\tilde{\mathbf{Z}}^{(k)}, \text{mask}(\tilde{\mathbf{x}}^{(k)} + \tilde{\mathbf{R}}^{(k)}; \overline{\mathbf{M}}^{(k)}))), \quad (4)$$

where $\hat{\mathbf{S}}^{(k)}$ denotes the reconstructed spatial positions. The loss L used to train our model combines the Mean Squared Error (MSE) reconstruction losses over both decoders:

$$L = \sum_{k=1}^K \|\text{mask}(\mathbf{x}^{(k)} - \hat{\mathbf{x}}^{(k)}; \overline{\mathbf{M}}^{(k)})\|_2^2 + \|\text{mask}(\mathbf{S}^{(k)} - \hat{\mathbf{S}}^{(k)}; \overline{\mathbf{M}}^{(k)})\|_2^2. \quad (5)$$

Our dual reconstruction objectives compel the model to extract, utilize, and preserve the full spectrum of signal, spatial, and structural information.

A practical challenge in multi-modal, multi-node IoT systems is the frequent occurrence of missing data due to hardware failures or unreliable communication links. To mitigate their impact, we pad missing entries with zeros and exclude them from the reconstruction loss by setting their corresponding loss terms to zero.

3.3 Theoretical Analyses

In this subsection, we provide theoretical support for the design of SPAR, drawing from principles in both information theory and occlusion-invariant representation learning. These insights help illuminate the rationale behind SPAR's design.

Analysis from the Perspective of Information Theory. We first analyze SPAR in comparison to classical MAE through the lens of information theory, as formalized in the following proposition:

Proposition 3.1. *Let $\mathbf{X}^{(k)}, \tilde{\mathbf{Z}}^{(k)}, \mathbf{S}^{(k)}, \mathbf{R}^{(k)}$ denote the random variables corresponding to the signals, the post-fusion latent embeddings, the spatial positions, and the structural positions, for $k \in \{1, \dots, K\}$, respectively. Let $\mathbb{E}[L']$ and $\mathbb{E}[L]$ denote the expected losses of classical MAE and SPAR over the data distribution, respectively, and let C' and C be constants independent of model parameters. Then, under certain assumptions, for classical MAE, we can have the following bound:*

$$-\mathbb{E}[L'] + C' \leq \sum_{k=1}^K I(\mathbf{X}^{(k)}; \tilde{\mathbf{Z}}^{(k)}), \quad (6)$$

where $I(\cdot; \cdot)$ denotes mutual information. In contrast, for SPAR, we can have

$$-\mathbb{E}[L] + C \leq \sum_{k=1}^K I(\mathbf{X}^{(k)}; \tilde{\mathbf{Z}}^{(k)} | \mathbf{S}^{(k)}, \mathbf{R}^{(k)}) + I(\mathbf{S}^{(k)}; \tilde{\mathbf{Z}}^{(k)} | \mathbf{X}^{(k)}, \mathbf{R}^{(k)}). \quad (7)$$

where $I(\cdot; \cdot | \cdot)$ denotes conditional mutual information.

The proof is detailed in Appendix B.1. This result highlights a key distinction between classical MAE and SPAR. In classical MAE, minimizing the expected loss encourages latent embeddings to retain information about the input signals, but without explicitly incorporating spatial or structural context. In contrast, SPAR is designed to promote embeddings that capture signal information beyond what is explained by structural and spatial cues, and similarly, to retain spatial information conditioned on the signal and structural characteristics. This encourages the embeddings to be context-aware and jointly informative of both signals and spatial layout, while avoiding memorizing redundant information.

Analysis from the Perspective of Occlusion-invariant Representation. We next analyze SPAR through the lens of occlusion-invariant representation learning. For clarity and readability, we present the analysis for a single modality by omitting the superscript (k) ; the generalization to the multi-modality case is straightforward. The core result is formalized in the following proposition:

Proposition 3.2. *As shown by Kong et al. [31], classical MAE can be viewed as a form of contrastive learning, where the positive pair consists of two complementary masked views of the signals:*

$$[\text{mask}(\mathcal{X}; M), \text{mask}(\mathcal{X}; \overline{M})]. \quad (8)$$

In contrast, SPAR can be interpreted as performing contrastive learning over two types of enriched positive pairs: 1) complementary masked views of signals with shared spatial and structural context:

$$[(\text{mask}(\mathcal{X}; M), \mathcal{S}, \mathcal{R}), (\text{mask}(\mathcal{X}; \overline{M}), \mathcal{S}, \mathcal{R})], \quad (9)$$

and 2) complementary masked views of spatial positions with shared signal and structural context:

$$[(\mathcal{X}, \text{mask}(\mathcal{S}; M), \mathcal{R}), (\mathcal{X}, \text{mask}(\mathcal{S}; \overline{M}), \mathcal{R})]. \quad (10)$$

The proof is detailed in Appendix B.2. This formulation highlights another key distinction: by treating masked views of the signal embeddings as positive pairs, classical MAE promotes occlusion-invariant representations solely within the signal domain, without accounting for spatial or structural positions. In contrast, SPAR encourages representations to be invariant to occlusion in both the signal and spatial domains, while preserving the presence of each other and the structural characteristics, leading to more robust and context-aware learned representations.

4 Evaluation

In this section, we present our experimental evaluation of SPAR on three multiple multi-modal, multi-node IoT datasets spanning diverse sensing modalities and spatial scales. To ensure a fair comparison, all baseline methods and our model use the same ViT backbone architecture [13] and identical task-specific prediction heads. Pretraining and fine-tuning are conducted for the same number of epochs across all methods. All reported results are aggregated over three random seeds. The prediction heads are designed to be lightweight and straightforward, tailored to the needs of each downstream task. Detailed descriptions of each task setup can be found in Appendix C.

Datasets. We conducted experiments on three real-world IoT datasets: (1) the M3N-VC dataset[34], which includes acoustic and seismic signals from moving vehicles, collected across six distinct outdoor scenes; (2) the Ridgecrest Seismicity Dataset[5], containing multi-modal seismic waveform recordings of earthquake events in the Ridgecrest region of California; and (3) the RealWorld-HAR dataset[58], comprising accelerometer, gyroscope, and magnetometer readings for human activity recognition. Further dataset details are available in Appendix C.

Baselines. We compare SPAR against eight state-of-the-art baseline methods: CMC [60], Cosmo [48], SimCLR [9], AudioMAE [24], CAV-MAE [18], FOCAL [41], FreqMAE [28], and PhyMask [27]. Among these, CMC, Cosmo, SimCLR, and FOCAL are contrastive learning-based methods, while AudioMAE, CAV-MAE, and FreqMAE follow the masked autoencoding (MAE) paradigm. Please see Appendix C.1 for a detailed description of each baseline.

4.1 Evaluation on M3N-VC Dataset

We begin our evaluation with the M3N-VC dataset, focusing on the task of **single-vehicle localization**, where the goal is to predict the location of a vehicle within the monitored area. In this setting, we pretrain on the full dataset and finetune only the prediction head (a single transformer layer) on the scene "H24", which contains a single moving vehicle. To evaluate the robustness of SPAR under

Table 1: Comparison of the MSE and averaged Distance Error between SPAR and baselines on M3N-VC single-vehicle localization task. The label ratio during fine-tuning varies from 1.0 to 0.2.

Method	M3N-VC Single-vehicle Localization					
	Label Ratio 1.0		Label Ratio 0.5		Label Ratio 0.2	
	MSE (m^2) (↓)	Dist. Err. (m) (↓)	MSE (m^2) (↓)	Dist. Err. (m) (↓)	MSE (m^2) (↓)	Dist. Err. (m) (↓)
CMC	51.11 ± 14.67	6.76 ± 0.75	71.81 ± 15.32	7.99 ± 0.64	111.37 ± 8.02	11.05 ± 0.57
Cosmo	38.40 ± 4.14	6.03 ± 0.21	53.12 ± 9.75	7.19 ± 0.40	97.08 ± 9.49	10.95 ± 0.57
SimCLR	34.40 ± 4.47	5.64 ± 0.25	45.14 ± 7.34	6.57 ± 0.08	74.53 ± 3.13	9.48 ± 0.17
AudioMAE	22.36 ± 0.49	5.40 ± 0.11	30.12 ± 2.97	6.33 ± 0.28	41.75 ± 3.30	7.47 ± 0.28
CAV-MAE	18.85 ± 0.41	5.06 ± 0.04	22.90 ± 0.82	5.58 ± 0.12	24.84 ± 0.33	5.78 ± 0.10
FOCAL	32.43 ± 4.68	5.37 ± 0.22	40.84 ± 2.82	6.20 ± 0.19	69.62 ± 5.62	8.50 ± 0.35
FreqMAE	29.61 ± 2.85	5.36 ± 0.16	42.06 ± 14.44	6.25 ± 0.70	91.40 ± 35.32	9.15 ± 1.27
PhyMask	28.02 ± 5.91	5.29 ± 0.33	33.74 ± 2.18	5.85 ± 0.12	64.36 ± 4.70	8.44 ± 0.36
SPAR	12.98 ± 0.11	4.20 ± 0.07	15.07 ± 1.03	4.51 ± 0.09	21.36 ± 0.62	5.40 ± 0.04

Table 2: Comparison of the mAP@ r metric (r is the distance threshold varying across $\{2,4,6,8\}$ meters) between SPAR and baselines on M3N-VC multi-vehicle joint classification and localization task.

Method	M3N-VC Multi-vehicle Joint Classification and Localization			
	mAP@4m (%) (↑)	mAP@6m (%) (↑)	mAP@8m (%) (↑)	mAP@10m (%) (↑)
CMC	0.06 ± 0.05	0.48 ± 0.36	1.61 ± 1.10	3.62 ± 2.19
Cosmo	0.16 ± 0.05	1.66 ± 0.23	4.77 ± 0.72	9.52 ± 1.20
SimCLR	0.31 ± 0.14	2.22 ± 0.58	6.53 ± 1.24	13.07 ± 2.08
AudioMAE	1.39 ± 0.48	6.96 ± 1.42	17.11 ± 3.24	28.98 ± 4.01
CAV-MAE	22.12 ± 2.94	52.08 ± 4.16	73.41 ± 3.24	85.36 ± 1.78
FOCAL	0.08 ± 0.05	0.82 ± 0.40	2.94 ± 1.04	6.82 ± 1.99
FreqMAE	0.24 ± 0.01	1.67 ± 0.32	5.34 ± 0.99	11.31 ± 1.49
PhyMask	0.08 ± 0.03	0.88 ± 0.24	3.04 ± 0.74	6.64 ± 1.46
SPAR	41.57 ± 2.69	71.82 ± 3.69	86.28 ± 1.77	92.99 ± 0.79

limited supervision, we vary the ratio of labeled data used during fine-tuning, ranging from 100% to 20%. Results are presented in Table 1. Across all label ratios, SPAR consistently achieves the lowest MSE and average Distance Error, demonstrating both strong empirical performance and notable resilience to scarce supervision. To facilitate intuitive understanding, we provide a visualization of the predicted vehicle locations in Appendix D.1.

We next evaluate SPAR on a more challenging task: **multi-vehicle joint classification and localization**, where the model must simultaneously classify and localize multiple vehicles moving concurrently in the field, despite the superposition of their generated signals. Similarly, we pretrain on the full dataset and finetune on the scene "I22", which includes multiple moving vehicles. To achieve this, we choose a 2-layer transformer as the task head, supervised with a DETR-style loss function [6]. To assess the performance, we adapt the metric mAP@ r (mean Average Precision at distance threshold r) from visual object detection literature [39]. mAP@ r computes the mean of the average precision (AP) scores across all vehicle classes, where a prediction is considered correct only if the predicted vehicle class is accurate and the predicted location falls within distance r of the ground-truth. As shown in Table 2, SPAR outperforms all baselines across a range of distance thresholds, including strict ones such as 4 meters—despite the low-resolution (1Hz) and noisy GPS ground truth obtained from smartphones. These results highlight the model's strong capability for spatial reasoning under complex conditions. To aid understanding of our experimental setup, the mAP@ r metric, and SPAR's performance, we include visualization examples in Appendix D.1.

To further assess generalizability, we conduct four additional evaluations on this dataset (details in Appendix D.1): (1) **Single-vehicle Classification**: We compare the performance between SPAR and baselines on classifying individual vehicles. As shown in Table 5, SPAR achieves the highest accuracy and F1 score across all baselines. (2) **Lossy Communication Scenario**: We simulate a setting with random node-level data dropout to mimic lossy communication networks. Results in Table 6 demonstrate that SPAR shows notable robustness to missing data, and maintains stronger performance than baselines. (3) **Generalization to Unseen Sensor Placements**: We test whether pretrained encoders (kept frozen) generalize to new sensor placements unseen during pretraining. As

Table 3: Comparison of the MSE and averaged Distance Error between SPAR and baselines on Ridgecrest Seismicity Dataset earthquake localization task (left). And comparison of the Accuracy and F1 score between SPAR and baselines on RealWorld-HAR human activity recognition task (right).

Method	Ridgecrest Seismicity Dataset Earthquake Localization		Realworld-HAR Activity Recognition	
	MSE (km^2) (↓)	Dist. Err. (km) (↓)	Accuracy (%) (↑)	F1 (%) (↑)
CMC	94.25 ± 6.67	10.38 ± 0.63	74.97 ± 1.23	74.82 ± 2.18
Cosmo	98.24 ± 13.77	10.44 ± 0.83	84.37 ± 0.33	85.30 ± 0.43
SimCLR	99.87 ± 11.31	10.29 ± 0.52	84.36 ± 0.47	85.49 ± 0.36
AudioMAE	33.65 ± 3.51	5.65 ± 0.29	89.18 ± 0.32	90.11 ± 0.53
CAV-MAE	31.58 ± 3.57	5.48 ± 0.37	88.12 ± 0.24	89.05 ± 0.35
FOCAL	131.50 ± 1.48	12.53 ± 0.09	84.98 ± 0.73	86.24 ± 0.77
FreqMAE	54.08 ± 5.44	7.14 ± 0.25	83.43 ± 0.56	84.07 ± 0.50
PhyMask	56.39 ± 3.27	7.67 ± 0.39	84.79 ± 3.23	82.15 ± 9.13
SPAR	23.46 ± 2.77	5.37 ± 0.24	89.63 ± 0.57	90.45 ± 0.63

shown in Table 7, SPAR achieves strong performance even in this challenging setting, outperforming all baselines, affirming its placement-aware generalization ability. (4) **Ablation Study**: Finally, we perform ablation studies to evaluate the contribution of each design component in SPAR. Table 8 confirms that each component contributes meaningfully, and the full model yields the strongest performance, demonstrating a synergistic effect.

4.2 Evaluation on Ridgecrest Seismicity Dataset

In the subsequent experiment, we evaluate SPAR on the Ridgecrest Seismicity Dataset, focusing on the task of earthquake event localization. Given multi-modal seismic waveform signals collected from 16 monitoring stations, the goal is to predict the 3D coordinates of each earthquake event. This task presents unique challenges compared to the vehicle monitoring scenario. Notably, the spatial scale is significantly larger—spanning tens of kilometers—and the dataset exhibits an inherent 20.38% missing data rate, primarily due to weak seismic waves failing to propagate to distant stations. Despite these challenges, SPAR achieves the best overall performance, as shown in Table 3, obtaining the lowest MSE and Distance Error among all methods. These results further demonstrate the model’s strong spatial reasoning capabilities in large-scale, partially observed environments. We provide additional visualizations of the localization predictions in Appendix D.2 to help illustrate the effectiveness of SPAR.

4.3 Evaluation on RealWorld-HAR Dataset

Finally, we evaluate SPAR on the RealWorld-HAR dataset to examine its robustness in IMU-based human activity recognition. This task presents a distinct set of challenges: it operates on a relatively small spatial scale but involves highly diverse structural positions, as sensors are mounted on different parts of the human body (e.g., wrist, ankle, chest), each generating signals with drastically different patterns. Despite this variability, SPAR achieves the highest accuracy and F1 scores among all compared methods, as reported in Table 3, underscoring its effectiveness in handling heterogeneous sensor characteristics. To further analyze model behavior, we provide a visualization of the classification confusion matrix in Appendix D.3.

5 Conclusion

This paper presents SPAR, a self-supervised pretraining framework designed for multi-modal, multi-node IoT systems. By introducing spatial and structural positional embeddings alongside dual reconstruction objectives, SPAR leverages the inherent duality between observer positions and observed signals to enable placement-aware representation learning. Theoretical analyses grounded in information theory and occlusion-invariant learning offer principled support for the framework. Extensive experiments across three real-world datasets—spanning diverse sensing modalities, placement configurations, and task types—demonstrate the superior generalizability and robustness of SPAR. We discuss the limitations of our current approach and outline directions for future work in Appendix E. We hope this work inspires broader efforts toward integrating spatial and structural context into foundational representation learning paradigms for intelligent IoT systems.

References

- [1] United States. Defense Mapping Agency. *Department of Defense World Geodetic System 1984: its definition and relationships with local geodetic systems*, volume 8350. Defense Mapping Agency, 1987.
- [2] Ozan Baris, Yizhuo Chen, Gaofeng Dong, Liying Han, Tomoyoshi Kimura, Pengrui Quan, Ruijie Wang, Tianchen Wang, Tarek Abdelzaher, Mario Bergés, et al. Foundation models for cps-iot: Opportunities and challenges. *arXiv preprint arXiv:2501.16368*, 2025.
- [3] Gourav Bathla, Kishor Bhadane, Rahul Kumar Singh, Rajneesh Kumar, Rajanikanth Aluvalu, Rajalakshmi Krishnamurthi, Adarsh Kumar, RN Thakur, and Shakila Basheer. Autonomous vehicles and intelligent automation: Applications, challenges, and opportunities. *Mobile Information Systems*, 2022(1):7632892, 2022.
- [4] Jiang Bian, Abdullah Al Arafat, Haoyi Xiong, Jing Li, Li Li, Hongyang Chen, Jun Wang, Dejing Dou, and Zhishan Guo. Machine learning in real-time internet of things (iot) systems: A survey. *IEEE Internet of Things Journal*, 9(11):8364–8386, 2022.
- [5] California Institute of Technology (Caltech). Southern california seismic network. Other/Seismic Network, 1926.
- [6] Nicolas Carion, Francisco Massa, Gabriel Synnaeve, Nicolas Usunier, Alexander Kirillov, and Sergey Zagoruyko. End-to-end object detection with transformers. In *European conference on computer vision*, pages 213–229. Springer, 2020.
- [7] Mathilde Caron, Neil Houlsby, and Cordelia Schmid. Location-aware self-supervised transformers for semantic segmentation. In *Proceedings of the IEEE/CVF Winter Conference on Applications of Computer Vision*, pages 117–127, 2024.
- [8] Earthquake Center. Southern california earthquake center. *Caltech. Dataset*, 394, 2013.
- [9] Ting Chen, Simon Kornblith, Mohammad Norouzi, and Geoffrey Hinton. A simple framework for contrastive learning of visual representations. In *International conference on machine learning*, pages 1597–1607. PmLR, 2020.
- [10] Abhimanyu Das, Weihao Kong, Rajat Sen, and Yichen Zhou. A decoder-only foundation model for time-series forecasting. In *Forty-first International Conference on Machine Learning*, 2024.
- [11] Shohreh Deldari, Hao Xue, Aaqib Saeed, Daniel V Smith, and Flora D Salim. Cocoa: Cross modality contrastive learning for sensor data. *Proceedings of the ACM on Interactive, Mobile, Wearable and Ubiquitous Technologies*, 6(3):1–28, 2022.
- [12] Carl Doersch, Abhinav Gupta, and Alexei A Efros. Unsupervised visual representation learning by context prediction. In *Proceedings of the IEEE international conference on computer vision*, pages 1422–1430, 2015.
- [13] Alexey Dosovitskiy, Lucas Beyer, Alexander Kolesnikov, Dirk Weissenborn, Xiaohua Zhai, Thomas Unterthiner, Mostafa Dehghani, Matthias Minderer, Georg Heigold, Sylvain Gelly, et al. An image is worth 16x16 words: Transformers for image recognition at scale. *arXiv preprint arXiv:2010.11929*, 2020.
- [14] Christoph Feichtenhofer, Yanghao Li, Kaiming He, et al. Masked autoencoders as spatiotemporal learners. *Advances in neural information processing systems*, 35:35946–35958, 2022.
- [15] Haotian Gao, Renhe Jiang, Zheng Dong, Jinliang Deng, Yuxin Ma, and Xuan Song. Spatial-temporal-decoupled masked pre-training for spatiotemporal forecasting. *arXiv preprint arXiv:2312.00516*, 2023.
- [16] Azul Garza, Cristian Challu, and Max Mergenthaler-Canseco. Timegpt-1. *arXiv preprint arXiv:2310.03589*, 2023.

[17] Rohit Girdhar, Alaaeldin El-Nouby, Zhuang Liu, Mannat Singh, Kalyan Vasudev Alwala, Armand Joulin, and Ishan Misra. Imagebind: One embedding space to bind them all. In *Proceedings of the IEEE/CVF conference on computer vision and pattern recognition*, pages 15180–15190, 2023.

[18] Yuan Gong, Andrew Rouditchenko, Alexander H Liu, David Harwath, Leonid Karlinsky, Hilde Kuehne, and James Glass. Contrastive audio-visual masked autoencoder. *arXiv preprint arXiv:2210.07839*, 2022.

[19] Mononito Goswami, Konrad Szafer, Arjun Choudhry, Yifu Cai, Shuo Li, and Artur Dubrawski. Moment: A family of open time-series foundation models. *arXiv preprint arXiv:2402.03885*, 2024.

[20] Nate Gruver, Marc Finzi, Shikai Qiu, and Andrew G Wilson. Large language models are zero-shot time series forecasters. *Advances in Neural Information Processing Systems*, 36:19622–19635, 2023.

[21] Fuqiang Gu, Mu-Huan Chung, Mark Chignell, Shahrokh Valaei, Baoding Zhou, and Xue Liu. A survey on deep learning for human activity recognition. *ACM Computing Surveys (CSUR)*, 54(8):1–34, 2021.

[22] Pengfei Gu, Yejia Zhang, Huimin Li, Chaoli Wang, and Danny Z Chen. Self pre-training with topology-and spatiality-aware masked autoencoders for 3d medical image segmentation. *arXiv preprint arXiv:2406.10519*, 2024.

[23] Kaiming He, Xinlei Chen, Saining Xie, Yanghao Li, Piotr Dollár, and Ross Girshick. Masked autoencoders are scalable vision learners. In *Proceedings of the IEEE/CVF conference on computer vision and pattern recognition*, pages 16000–16009, 2022.

[24] Po-Yao Huang, Hu Xu, Juncheng Li, Alexei Baevski, Michael Auli, Wojciech Galuba, Florian Metze, and Christoph Feichtenhofer. Masked autoencoders that listen. *Advances in Neural Information Processing Systems*, 35:28708–28720, 2022.

[25] Jeremy Irvin, Lucas Tao, Joanne Zhou, Yuntao Ma, Langston Nashold, Benjamin Liu, and Andrew Y Ng. Usat: A unified self-supervised encoder for multi-sensor satellite imagery. *arXiv preprint arXiv:2312.02199*, 2023.

[26] Charmi Jobanputra, Jatna Bavishi, and Nishant Doshi. Human activity recognition: A survey. *Procedia Computer Science*, 155:698–703, 2019.

[27] Denizhan Kara, Tomoyoshi Kimura, Yatong Chen, Jinyang Li, Ruijie Wang, Yizhuo Chen, Tian-shi Wang, Shengzhong Liu, and Tarek Abdelzaher. Phymask: An adaptive masking paradigm for efficient self-supervised learning in iot. In *Proceedings of the 22nd ACM Conference on Embedded Networked Sensor Systems*, pages 97–111, 2024.

[28] Denizhan Kara, Tomoyoshi Kimura, Shengzhong Liu, Jinyang Li, Dongxin Liu, Tianshi Wang, Ruijie Wang, Yizhuo Chen, Yigong Hu, and Tarek Abdelzaher. Freqmae: Frequency-aware masked autoencoder for multi-modal iot sensing. In *Proceedings of the ACM Web Conference 2024*, pages 2795–2806, 2024.

[29] Bernhard Kerbl, Georgios Kopanas, Thomas Leimkühler, and George Drettakis. 3d gaussian splatting for real-time radiance field rendering. *ACM Trans. Graph.*, 42(4):139–1, 2023.

[30] Dahun Kim, Donghyeon Cho, Donggeun Yoo, and In So Kweon. Learning image representations by completing damaged jigsaw puzzles. In *2018 IEEE winter conference on applications of computer vision (WACV)*, pages 793–802. IEEE, 2018.

[31] Xiangwen Kong and Xiangyu Zhang. Understanding masked image modeling via learning occlusion invariant feature. In *Proceedings of the IEEE/CVF Conference on Computer Vision and Pattern Recognition*, pages 6241–6251, 2023.

[32] Zhenzhong Lan, Mingda Chen, Sebastian Goodman, Kevin Gimpel, Piyush Sharma, and Radu Soricut. Albert: A lite bert for self-supervised learning of language representations. *arXiv preprint arXiv:1909.11942*, 2019.

[33] Haejun Lee, Drew A Hudson, Kangwook Lee, and Christopher D Manning. Slm: Learning a discourse language representation with sentence unshuffling. *arXiv preprint arXiv:2010.16249*, 2020.

[34] Jinyang Li, Yizhuo Chen, Ruijie Wang, Tomoyoshi Kimura, Tianshi Wang, You Lyu, Hongjue Zhao, Binqi Sun, Shangchen Wu, Yigong Hu, Denizhan Kara, Beiting Tian, Klara Nahrstedt, Suhas Diggavi, Jae H. Kim, Greg Kimberly, Guijun Wang, Maggie Wigness, and Tarek Abdelzaher. RestoreML: Practical unsupervised tuning of deployed intelligent iot systems. In *2025 The 21st International Conference on Distributed Computing in Smart Systems and the Internet of Things (DCOSS-IoT)*. IEEE, 2025.

[35] Rui Li, Yiting Wang, Wei-Long Zheng, and Bao-Liang Lu. A multi-view spectral-spatial-temporal masked autoencoder for decoding emotions with self-supervised learning. In *Proceedings of the 30th ACM International Conference on Multimedia*, pages 6–14, 2022.

[36] Yanghao Li, Hanzi Mao, Ross Girshick, and Kaiming He. Exploring plain vision transformer backbones for object detection. In *European conference on computer vision*, pages 280–296. Springer, 2022.

[37] Zhe Li, Zhongwen Rao, Lujia Pan, Pengyun Wang, and Zenglin Xu. Ti-mae: Self-supervised masked time series autoencoders. *arXiv preprint arXiv:2301.08871*, 2023.

[38] Junyan Lin, Feng Gao, Xiaochen Shi, Junyu Dong, and Qian Du. Ss-mae: Spatial–spectral masked autoencoder for multisource remote sensing image classification. *IEEE Transactions on Geoscience and Remote Sensing*, 61:1–14, 2023.

[39] Tsung-Yi Lin, Michael Maire, Serge Belongie, James Hays, Pietro Perona, Deva Ramanan, Piotr Dollár, and C Lawrence Zitnick. Microsoft coco: Common objects in context. In *Computer vision–ECCV 2014: 13th European conference, zurich, Switzerland, September 6–12, 2014, proceedings, part v 13*, pages 740–755. Springer, 2014.

[40] Qian Liu, Junchen Ye, Haohan Liang, Leilei Sun, and Bowen Du. Ts-mae: A masked autoencoder for time series representation learning. *Information Sciences*, 690:121576, 2025.

[41] Shengzhong Liu, Tomoyoshi Kimura, Dongxin Liu, Ruijie Wang, Jinyang Li, Suhas Diggavi, Mani Srivastava, and Tarek Abdelzaher. Focal: Contrastive learning for multimodal time-series sensing signals in factorized orthogonal latent space. *Advances in Neural Information Processing Systems*, 36:47309–47338, 2023.

[42] Yinhan Liu, Myle Ott, Naman Goyal, Jingfei Du, Mandar Joshi, Danqi Chen, Omer Levy, Mike Lewis, Luke Zettlemoyer, and Veselin Stoyanov. Roberta: A robustly optimized bert pretraining approach. *arXiv preprint arXiv:1907.11692*, 2019.

[43] Shenghuan Miao, Ling Chen, and Rong Hu. Spatial-temporal masked autoencoder for multi-device wearable human activity recognition. *Proceedings of the ACM on Interactive, Mobile, Wearable and Ubiquitous Technologies*, 7(4):1–25, 2024.

[44] Ben Mildenhall, Pratul P Srinivasan, Matthew Tancik, Jonathan T Barron, Ravi Ramamoorthi, and Ren Ng. Nerf: Representing scenes as neural radiance fields for view synthesis. *Communications of the ACM*, 65(1):99–106, 2021.

[45] Shentong Mo, Russ Salakhutdinov, Louis-Philippe Morency, and Paul Pu Liang. Iot-lm: Large multisensory language models for the internet of things. *arXiv preprint arXiv:2407.09801*, 2024.

[46] Abhilash Nandy, Yash Kulkarni, Pawan Goyal, and Niloy Ganguly. Order-based pre-training strategies for procedural text understanding. *arXiv preprint arXiv:2404.04676*, 2024.

[47] Mehdi Noroozi and Paolo Favaro. Unsupervised learning of visual representations by solving jigsaw puzzles. In *European conference on computer vision*, pages 69–84. Springer, 2016.

[48] Xiaomin Ouyang, Xian Shuai, Jiayu Zhou, Ivy Wang Shi, Zhiyuan Xie, Guoliang Xing, and Jianwei Huang. Cosmo: contrastive fusion learning with small data for multimodal human activity recognition. In *Proceedings of the 28th Annual International Conference on Mobile Computing And Networking*, pages 324–337, 2022.

[49] Xiaomin Ouyang and Mani Srivastava. Llmsense: Harnessing llms for high-level reasoning over spatiotemporal sensor traces. In *2024 IEEE 3rd Workshop on Machine Learning on Edge in Sensor Systems (SenSys-ML)*, pages 9–14. IEEE, 2024.

[50] Xiaomin Ouyang, Jason Wu, Tomoyoshi Kimura, Yihan Lin, Gunjan Verma, Tarek Abdelzaher, and Mani Srivastava. Mmbind: Unleashing the potential of distributed and heterogeneous data for multimodal learning in iot. *arXiv preprint arXiv:2411.12126*, 2024.

[51] Ofir Press, Noah A Smith, and Mike Lewis. Train short, test long: Attention with linear biases enables input length extrapolation. *arXiv preprint arXiv:2108.12409*, 2021.

[52] Colorado J Reed, Ritwik Gupta, Shufan Li, Sarah Brockman, Christopher Funk, Brian Clipp, Kurt Keutzer, Salvatore Candido, Matt Uyttendaele, and Trevor Darrell. Scale-mae: A scale-aware masked autoencoder for multiscale geospatial representation learning. In *Proceedings of the IEEE/CVF International Conference on Computer Vision*, pages 4088–4099, 2023.

[53] Rodrigo Santa Cruz, Basura Fernando, Anoop Cherian, and Stephen Gould. Deeppermnet: Visual permutation learning. In *Proceedings of the IEEE Conference on Computer Vision and Pattern Recognition*, pages 3949–3957, 2017.

[54] Xu Si, Xinming Wu, Zefeng Li, Shenghou Wang, and Jun Zhu. An all-in-one seismic phase picking, location, and association network for multi-task multi-station earthquake monitoring. *Communications Earth & Environment*, 5(1):22, 2024.

[55] Jianlin Su, Murtadha Ahmed, Yu Lu, Shengfeng Pan, Wen Bo, and Yunfeng Liu. Roformer: Enhanced transformer with rotary position embedding. *Neurocomputing*, 568:127063, 2024.

[56] Yuancheng Sun, Kai Chen, Kang Liu, and Qiwei Ye. 3d molecular pretraining via localized geometric generation. *bioRxiv*, pages 2024–09, 2024.

[57] Abbas Shah Syed, Daniel Sierra-Sosa, Anup Kumar, and Adel Elmaghraby. Iot in smart cities: A survey of technologies, practices and challenges. *Smart Cities*, 4(2):429–475, 2021.

[58] Timo Szttyler and Heiner Stuckenschmidt. On-body localization of wearable devices: An investigation of position-aware activity recognition. In *2016 IEEE international conference on pervasive computing and communications (PerCom)*, pages 1–9. IEEE, 2016.

[59] Xiaoyu Tian, Haoxi Ran, Yue Wang, and Hang Zhao. Geomae: Masked geometric target prediction for self-supervised point cloud pre-training. In *Proceedings of the IEEE/CVF Conference on Computer Vision and Pattern Recognition*, pages 13570–13580, 2023.

[60] Yonglong Tian, Dilip Krishnan, and Phillip Isola. Contrastive multiview coding. In *Computer Vision–ECCV 2020: 16th European Conference, Glasgow, UK, August 23–28, 2020, Proceedings, Part XI 16*, pages 776–794. Springer, 2020.

[61] Silvia Liberata Ullo and Ganesh Ram Sinha. Advances in smart environment monitoring systems using iot and sensors. *Sensors*, 20(11):3113, 2020.

[62] Ashish Vaswani, Noam Shazeer, Niki Parmar, Jakob Uszkoreit, Llion Jones, Aidan N Gomez, Łukasz Kaiser, and Illia Polosukhin. Attention is all you need. *Advances in neural information processing systems*, 30, 2017.

[63] W Wang, B Bi, M Yan, C Wu, Z Bao, and J Xia. Structbert: Incorporating language structures into pre-training for deep language understanding. eprint. *arXiv preprint arXiv:1908.04577*, 2019.

[64] Gerald Woo, Chenghao Liu, Akshat Kumar, Caiming Xiong, Silvio Savarese, and Doyen Sahoo. Unified training of universal time series forecasting transformers. 2024.

[65] Guanjun Wu, Taoran Yi, Jiemin Fang, Lingxi Xie, Xiaopeng Zhang, Wei Wei, Wenyu Liu, Qi Tian, and Xinggang Wang. 4d gaussian splatting for real-time dynamic scene rendering. In *Proceedings of the IEEE/CVF conference on computer vision and pattern recognition*, pages 20310–20320, 2024.

- [66] Qiangqiang Wu, Tianyu Yang, Ziquan Liu, Baoyuan Wu, Ying Shan, and Antoni B Chan. Dropmae: Masked autoencoders with spatial-attention dropout for tracking tasks. In *Proceedings of the IEEE/CVF conference on computer vision and pattern recognition*, pages 14561–14571, 2023.
- [67] Wenhan Wu, Yilei Hua, Ce Zheng, Shiqian Wu, Chen Chen, and Aidong Lu. Skeletonmae: Spatial-temporal masked autoencoders for self-supervised skeleton action recognition. In *2023 IEEE international conference on multimedia and expo workshops (ICMEW)*, pages 224–229. IEEE, 2023.
- [68] Huatao Xu, Liying Han, Qirui Yang, Mo Li, and Mani Srivastava. Penetrative ai: Making llms comprehend the physical world. In *Proceedings of the 25th International Workshop on Mobile Computing Systems and Applications*, pages 1–7, 2024.
- [69] Huatao Xu, Pengfei Zhou, Rui Tan, Mo Li, and Guobin Shen. Limu-bert: Unleashing the potential of unlabeled data for imu sensing applications. In *Proceedings of the 19th ACM Conference on Embedded Networked Sensor Systems*, pages 220–233, 2021.
- [70] Ke Yi, Yansen Wang, Kan Ren, and Dongsheng Li. Learning topology-agnostic eeg representations with geometry-aware modeling. *Advances in Neural Information Processing Systems*, 36:53875–53891, 2023.
- [71] Shuangfei Zhai, Navdeep Jaitly, Jason Ramapuram, Dan Busbridge, Tatiana Likhomanenko, Joseph Yitan Cheng, Walter Talbott, Chen Huang, Hanlin Goh, and Joshua Susskind. Position prediction as an effective pretraining strategy. *arXiv preprint arXiv:2207.07611*, 2022.

Appendix

A Notation Table

For the reader’s convenience, we provide a summary of the notations used throughout the paper, along with their corresponding dimensions and definitions, in Table 4.

Table 4: Summary of the notations and their corresponding dimensions and definitions.

Notation	Dimension(s)	Definition
K	\mathbb{N}	Number of modalities
$n^{(k)}, m^{(k)}, m_M^{(k)}$	\mathbb{N}	Number of nodes, tokens, and masked tokens
$d, d_{\mathcal{X}}^{(k)}$	\mathbb{N}	Model dimension, tokenized signal dimension
d_S, d_R	\mathbb{N}	Spatial and structural position dimensions
L, L'	\mathbb{N}	Loss function of SPAR and classical MAE
$\mathcal{X}^{(k)}$	$\mathbb{R}^{n^{(k)} \times m^{(k)} \times d_{\mathcal{X}}^{(k)}}$	Signals
$\widehat{\mathcal{X}}^{(k)}$	$\mathbb{R}^{n^{(k)} \times m^{(k)} \times d_{\mathcal{X}}^{(k)}}$	Reconstructed signals
$X^{(k)}$	$\mathbb{R}^{n^{(k)} \times m^{(k)} \times d_{\mathcal{X}}^{(k)}}$	Signals random variable
$\tilde{\mathcal{X}}^{(k)}$	$\mathbb{R}^{n^{(k)} \times m^{(k)} \times d}$	Signal embeddings
$S^{(k)}$	$\mathbb{R}^{n^{(k)} \times d_S}$	Spatial positions
$\mathcal{S}^{(k)}$	$\mathbb{R}^{n^{(k)} \times m^{(k)} \times d_S}$	Spatial positions (broadcasted)
$\widehat{\mathcal{S}}^{(k)}$	$\mathbb{R}^{n^{(k)} \times m^{(k)} \times d_S}$	Reconstructed spatial positions
$S^{(k)}$	$\mathbb{R}^{n^{(k)} \times m^{(k)} \times d_S}$	Spatial positions random variable
$\tilde{\mathcal{S}}^{(k)}$	$\mathbb{R}^{n^{(k)} \times m^{(k)} \times d}$	Spatial positional embeddings
$R^{(k)}$	$\mathbb{R}^{n^{(k)} \times d_R}$	Structural positions
$\mathcal{R}^{(k)}$	$\mathbb{R}^{n^{(k)} \times m^{(k)} \times d_R}$	Structural positions (broadcasted)
$R^{(k)}$	$\mathbb{R}^{n^{(k)} \times m^{(k)} \times d_R}$	Structural positions random variable
$\tilde{\mathcal{R}}^{(k)}$	$\mathbb{R}^{n^{(k)} \times m^{(k)} \times d}$	Structural positional embeddings
$M^{(k)}$	$\{0, 1\}^{n^{(k)} \times m^{(k)}}$	Mask
$\overline{M}^{(k)}$	$\{0, 1\}^{n^{(k)} \times m^{(k)}}$	Complement mask
$Z^{(k)}$	$\mathbb{R}^{m_M^{(k)} \times d}$	Pre-fusion latent embeddings
$\tilde{Z}^{(k)}$	$\mathbb{R}^{m_M^{(k)} \times d}$	Post-fusion latent embeddings
$\tilde{Z}^{(k)}$	$\mathbb{R}^{m_M^{(k)} \times d}$	Post-fusion latent embeddings random variable

B Proofs

B.1 Proof of Proposition 3.1

Proof. In this proof we use C and C' to denote generic constants independent of model parameters, whose specific values may change from Equation to Equation.

Classical MAE. We begin with the case of classical MAE. We assume, following prior works [36, 31], that due to the high dimension of the latent embeddings relative to the original signal, the latent embeddings $\tilde{Z}^{(k)}$ may contain the full information about the unmasked part of the signals $\text{mask}(\mathcal{X}^{(k)}; M^{(k)})$, which can be reconstructed by the decoder from the latent embeddings with negligible loss. As a result, we consider the reconstruction loss calculated on the masked signals to

be equivalent to the reconstruction loss calculated on the full signals:

$$\begin{aligned}
L' &= \sum_{k=1}^K \|\text{mask}(\mathbf{x}^{(k)} - \hat{\mathbf{x}}^{(k)}; \bar{\mathbf{M}}^{(k)})\|_2^2 \\
&= \sum_{k=1}^K \|\mathbf{x}^{(k)} - \hat{\mathbf{x}}^{(k)}\|_2^2 \\
&= \sum_{k=1}^K L'^{(k)},
\end{aligned} \tag{11}$$

where $L'^{(k)}$ is the reconstruction loss calculated for the k -th modality.

Like in the analysis for general regression tasks, the likelihood $P_{\text{dec}}(\mathbf{X}^{(k)} | \tilde{\mathbf{Z}}^{(k)} = \tilde{\mathbf{Z}}^{(k)})$ implicitly modeled by the decoder is defined as a fully factorized Gaussian distribution with mean $\hat{\mathbf{x}}^{(k)}$:

$$P_{\text{dec}}(\mathbf{X}^{(k)} | \tilde{\mathbf{Z}}^{(k)} = \tilde{\mathbf{Z}}^{(k)}) \stackrel{\text{def}}{=} \mathcal{N}(\hat{\mathbf{x}}^{(k)}, \frac{1}{\sqrt{2}}\mathbf{I}). \tag{12}$$

Then, we can interpret the MSE loss $L'^{(k)}$ as proportional to the negative log-likelihood:

$$\begin{aligned}
-\log P_{\text{dec}}(\mathbf{X}^{(k)} = \mathbf{x}^{(k)} | \tilde{\mathbf{Z}}^{(k)} = \tilde{\mathbf{Z}}^{(k)}) &= \|\mathbf{x}^{(k)} - \hat{\mathbf{x}}^{(k)}\|_2^2 + C' \\
&= L'^{(k)} + C'.
\end{aligned} \tag{13}$$

Since the prior probability $P(\mathbf{X}^{(k)} = \mathbf{x}^{(k)})$ is also a constant independent of the model parameters (only determined by the dataset distribution), we can further have

$$L'^{(k)} + C' = -\log \frac{P_{\text{dec}}(\mathbf{X}^{(k)} = \mathbf{x}^{(k)} | \tilde{\mathbf{Z}}^{(k)} = \tilde{\mathbf{Z}}^{(k)})}{P(\mathbf{X}^{(k)} = \mathbf{x}^{(k)})}. \tag{14}$$

Taking expectation over the data distribution and applying the standard mutual information decomposition, we can have:

$$\begin{aligned}
\mathbb{E}[L'^{(k)}] + C' &= \mathbb{E}[-\log \frac{P_{\text{dec}}(\mathbf{X}^{(k)} | \tilde{\mathbf{Z}}^{(k)})}{P(\mathbf{X}^{(k)})}] \\
&= \mathbb{E}[-\log \frac{P(\mathbf{X}^{(k)} | \tilde{\mathbf{Z}}^{(k)})}{P(\mathbf{X}^{(k)})} + \log \frac{P(\mathbf{X}^{(k)} | \tilde{\mathbf{Z}}^{(k)})}{P_{\text{dec}}(\mathbf{X}^{(k)} | \tilde{\mathbf{Z}}^{(k)})}] \\
&= -I(\mathbf{X}^{(k)}; \tilde{\mathbf{Z}}^{(k)}) + KL(P(\mathbf{X}^{(k)} | \tilde{\mathbf{Z}}^{(k)}) || P_{\text{dec}}(\mathbf{X}^{(k)} | \tilde{\mathbf{Z}}^{(k)})) \\
&\geq -I(\mathbf{X}^{(k)}; \tilde{\mathbf{Z}}^{(k)}),
\end{aligned} \tag{15}$$

where $P(\mathbf{X}^{(k)} | \tilde{\mathbf{Z}}^{(k)})$ denotes the non-tractable ground truth conditional distribution determined by the data distribution and the encoders, and $KL(\cdot || \cdot)$ denotes Kullback–Leibler divergence.

Summing over all modalities, we can prove:

$$-\mathbb{E}[L'] + C' \leq \sum_{k=1}^K I(\mathbf{X}^{(k)}; \tilde{\mathbf{Z}}^{(k)}). \tag{16}$$

SPAR. For SPAR, the signal decoder takes additional inputs: masked spatial and structural positional embeddings (Equation 3). Let $\mathbf{S}_M^{(k)}$ and $\mathbf{R}_M^{(k)}$ denote the masked spatial and structural positions. Let $L_{\text{sig}}^{(k)}$ denote the signal reconstruction loss for modality k . Then, adjusting our reasoning above, we can modify Equation 13 to:

$$L_{\text{sig}}^{(k)} + C = -\log P_{\text{dec}}(\mathbf{X}^{(k)} = \mathbf{x}^{(k)} | \tilde{\mathbf{Z}}^{(k)} = \tilde{\mathbf{Z}}^{(k)}, \mathbf{S}_M^{(k)} = \mathbf{s}_M^{(k)}, \mathbf{R}_M^{(k)} = \mathbf{r}_M^{(k)}). \tag{17}$$

Since in SPAR, the latent embeddings $\tilde{\mathbf{Z}}^{(k)}$ are calculated not only from unmasked signals, but also from unmasked spatial and structural positional embeddings, we can re-use our assumption above that the latent embeddings $\tilde{\mathbf{Z}}^{(k)}$ retain the full information of them. As a result, we can equivalently condition the likelihood on full spatial and structural positions:

$$\begin{aligned} L_{\text{sig}}^{(k)} + C &= -\log P_{\text{dec}}(\mathbf{X}^{(k)} = \mathcal{X}^{(k)} | \tilde{\mathbf{Z}}^{(k)} = \tilde{\mathbf{Z}}^{(k)}, \mathbf{S}_M^{(k)} = \mathcal{S}_M^{(k)}, \mathbf{R}_M^{(k)} = \mathcal{R}_M^{(k)}) \\ &= -\log P_{\text{dec}}(\mathbf{X}^{(k)} = \mathcal{X}^{(k)} | \tilde{\mathbf{Z}}^{(k)} = \tilde{\mathbf{Z}}^{(k)}, \mathbf{S}^{(k)} = \mathcal{S}^{(k)}, \mathbf{R}^{(k)} = \mathcal{R}^{(k)}). \end{aligned} \quad (18)$$

As the reasoning above, since the prior probability $P(\mathbf{X}^{(k)} = \mathcal{X}^{(k)} | \mathbf{S}^{(k)} = \mathcal{S}^{(k)}, \mathbf{R}^{(k)} = \mathcal{R}^{(k)})$ is also independent of the model parameters, we can adjust Equation 15 to:

$$\mathbb{E}[L_{\text{sig}}^{(k)}] + C \geq -I(\mathbf{X}^{(k)}; \tilde{\mathbf{Z}}^{(k)} | \mathbf{S}^{(k)}, \mathbf{R}^{(k)}). \quad (19)$$

Since SPAR treats spatial positions symmetrically to signals. We can apply the same reasoning on signal reconstruction loss to the spatial reconstruction loss $L_{\text{sp}}^{(k)}$, yielding:

$$\mathbb{E}[L_{\text{sp}}^{(k)}] + C \geq -I(\mathbf{S}^{(k)}; \tilde{\mathbf{Z}}^{(k)} | \mathbf{X}^{(k)}, \mathbf{R}^{(k)}). \quad (20)$$

Summing over all modalities and both reconstruction losses, we can prove:

$$-\mathbb{E}[L] + C \leq \sum_{k=1}^K I(\mathbf{X}^{(k)}; \tilde{\mathbf{Z}}^{(k)} | \mathbf{S}^{(k)}, \mathbf{R}^{(k)}) + I(\mathbf{S}^{(k)}; \tilde{\mathbf{Z}}^{(k)} | \mathbf{X}^{(k)}, \mathbf{R}^{(k)}). \quad (21)$$

□

B.2 Proof of Proposition 3.2

Proof. **Classical MAE.** Kong *et al.* [31] provided a rigorous interpretation of classical MAE as a special case of contrastive learning, where the positive pair consists of two complementary masked views of the same input signals. For completeness and clarity, we briefly restate their reasoning here using our notation. For clarity, we focus on a single modality by omitting the superscript (k) and the joint encoder $\mathcal{F}_{\text{joint_enc}}$; the extension to multiple modalities is straightforward.

Let $\mathcal{F}'_{\text{embed_enc}}$ denote the composition of the embedding layer and encoder in classical MAE, and let $\mathcal{F}'_{\text{dec}}$ denote the decoder. Then, the reconstruction process can be written as:

$$\hat{\mathcal{X}} = \mathcal{F}'_{\text{dec}}(\mathcal{F}'_{\text{embed_enc}}(\text{mask}(\mathcal{X}; \mathbf{M}))). \quad (22)$$

Accordingly, the reconstruction loss of classical MAE can be rewritten as

$$\begin{aligned} L' &= \|\text{mask}(\mathcal{X} - \hat{\mathcal{X}}; \overline{\mathbf{M}})\|_2^2 \\ &= \|\text{mask}(\mathcal{X}; \overline{\mathbf{M}}) - \text{mask}(\hat{\mathcal{X}}; \overline{\mathbf{M}})\|_2^2 \\ &= \|\text{mask}(\mathcal{X}; \overline{\mathbf{M}}) - \text{mask}(\mathcal{F}'_{\text{dec}}(\mathcal{F}'_{\text{embed_enc}}(\text{mask}(\mathcal{X}; \mathbf{M}))), \overline{\mathbf{M}})\|_2^2. \end{aligned} \quad (23)$$

Kong *et al.* [31] assumes that due to the high dimension of the latent embeddings relative to the original signals, the latent embeddings produced by the $\mathcal{F}'_{\text{embed_enc}}$ may approximately preserve all the information of the input. This implies the existence of an alternative decoder $\tilde{\mathcal{F}}'_{\text{dec}}$ that can satisfy:

$$\text{mask}(\mathcal{X}; \overline{\mathbf{M}}) \approx \text{mask}(\tilde{\mathcal{F}}'_{\text{dec}}(\mathcal{F}'_{\text{embed_enc}}(\text{mask}(\mathcal{X}; \overline{\mathbf{M}}))), \overline{\mathbf{M}}), \quad (24)$$

where $\tilde{\mathcal{F}}'_{\text{dec}}$ can be optimized as:

$$\begin{aligned} L_{\tilde{\mathcal{F}}'_{\text{dec}}} &= \|\text{mask}(\mathcal{X}; \overline{\mathbf{M}}) - \text{mask}(\tilde{\mathcal{F}}'_{\text{dec}}(\mathcal{F}'_{\text{embed_enc}}(\text{mask}(\mathcal{X}; \overline{\mathbf{M}}))), \overline{\mathbf{M}})\|_2^2 \\ \tilde{\mathcal{F}}'_{\text{dec}} &= \arg \min_{\tilde{\mathcal{F}}'_{\text{dec}}} \mathbb{E}[L_{\tilde{\mathcal{F}}'_{\text{dec}}}] \end{aligned} \quad (25)$$

Using this approximation, the classical MAE loss can be rewritten as:

$$\begin{aligned} L' \approx & \|\text{mask}(\tilde{\mathcal{F}}'_{\text{dec}}(\mathcal{F}'_{\text{embed_enc}}(\text{mask}(\mathcal{X}; \bar{M}))); \bar{M}) \\ & - \text{mask}(\mathcal{F}'_{\text{dec}}(\mathcal{F}'_{\text{embed_enc}}(\text{mask}(\mathcal{X}; M))); \bar{M})\|_2^2. \end{aligned} \quad (26)$$

To draw a connection to contrastive learning, we define the following similarity measure:

$$\mathcal{G}'(\mathcal{Z}_1, \mathcal{Z}_2) \stackrel{\text{def}}{=} \|\text{mask}(\tilde{\mathcal{F}}'_{\text{dec}}(\mathcal{Z}_1); \bar{M}) - \text{mask}(\mathcal{F}'_{\text{dec}}(\mathcal{Z}_2); \bar{M})\|_2^2. \quad (27)$$

Then the classical MAE loss can be rewritten as:

$$L' \approx \mathcal{G}'(\mathcal{F}'_{\text{embed_enc}}(\text{mask}(\mathcal{X}; \bar{M})), \mathcal{F}'_{\text{embed_enc}}(\text{mask}(\mathcal{X}; M))), \quad (28)$$

where $\mathcal{F}'_{\text{embed_enc}}$ is ensured non-trivial by Equation 25.

This reveals the contrastive learning view of classical MAE: L' encourages the encoder $\mathcal{F}'_{\text{embed_enc}}$ to produce similar latent representations from two complementary masked views of the same input signals:

$$[\text{mask}(\mathcal{X}; M), \text{mask}(\mathcal{X}; \bar{M})], \quad (29)$$

which explicitly promotes the learning of occlusion-invariant representations in the signal domain.

SPAR. We now turn to SPAR. To unify the components used in encoding, we define an extended encoder $\tilde{\mathcal{F}}_{\text{enc}}$ that encapsulates the signal, spatial, and structural embeddings, along with the encoder $\mathcal{F}_{\text{embed_enc}}$ and additional pre-decoder inputs:

$$\tilde{\mathcal{F}}_{\text{enc}}(\text{mask}(\mathcal{X}; M), \mathcal{S}, \mathcal{R}) \stackrel{\text{def}}{=} \left(\mathcal{F}_{\text{enc}}(\text{mask}(\mathcal{X} + \tilde{\mathcal{S}} + \tilde{\mathcal{R}}; M)), \text{mask}(\tilde{\mathcal{S}} + \tilde{\mathcal{R}}; \bar{M}) \right). \quad (30)$$

By the same logic as for classical MAE, we can assume the existence of a decoder $\tilde{\mathcal{F}}_{\text{sig_dec}}$ that reconstructs $\text{mask}(\mathcal{X}; \bar{M})$ almost losslessly from the output of $\tilde{\mathcal{F}}_{\text{enc}}$:

$$\text{mask}(\mathcal{X}; \bar{M}) \approx \text{mask}(\tilde{\mathcal{F}}_{\text{sig_dec}}(\tilde{\mathcal{F}}_{\text{enc}}(\text{mask}(\mathcal{X}; \bar{M}), \mathcal{S}, \mathcal{R})); \bar{M}). \quad (31)$$

We now define another similarity measure:

$$\mathcal{G}_{\text{sig}}(\mathcal{Z}_1, \mathcal{Z}_2) \stackrel{\text{def}}{=} \|\text{mask}(\tilde{\mathcal{F}}_{\text{sig_dec}}(\mathcal{Z}_1); \bar{M}) - \text{mask}(\mathcal{F}_{\text{sig_dec}}(\mathcal{Z}_2); \bar{M})\|_2^2. \quad (32)$$

Let L_{sig} denote the signal reconstruction loss in SPAR. Then we have the approximation similar to Equation 28:

$$L_{\text{sig}} \approx \mathcal{G}_{\text{sig}}(\tilde{\mathcal{F}}_{\text{enc}}(\text{mask}(\mathcal{X}; \bar{M}), \mathcal{S}, \mathcal{R}), \tilde{\mathcal{F}}_{\text{enc}}(\text{mask}(\mathcal{X}; M), \mathcal{S}, \mathcal{R})). \quad (33)$$

Following the same argument of Kong *et al.* [31], this shows that L_{sig} in SPAR can be viewed as a contrastive loss between two masked views of the signal, enriched with shared spatial and structural context:

$$[(\text{mask}(\mathcal{X}; M), \mathcal{S}, \mathcal{R}), (\text{mask}(\mathcal{X}; \bar{M}), \mathcal{S}, \mathcal{R})]. \quad (34)$$

Since SPAR treats spatial positions symmetrically with signals—both in embedding and reconstruction—we can apply the same reasoning to the spatial reconstruction loss L_{sp} . This yields another type of contrastive pair:

$$[(\mathcal{X}, \text{mask}(\mathcal{S}; M), \mathcal{R}), (\mathcal{X}, \text{mask}(\mathcal{S}; \bar{M}), \mathcal{R})]. \quad (35)$$

□

C Additional Experimental Setup

C.1 Baseline Methods Descriptions

Below, we provide detailed elaborations on the baseline methods introduced in Section 4.

CMC [60] Learns shared representations by maximizing mutual information between views, enabling view-agnostic and scalable contrastive learning across multiple modalities.

Cosmo [48] Integrates contrastive feature alignment with attention-based selective fusion to effectively capture shared and distinctive patterns from multimodal data under scarce labeling.

SimCLR [9] Forms discriminative visual embeddings by aligning augmented image pairs through a nonlinear projection and optimizing the NT-Xent contrastive loss.

AudioMAE [24] Applies masked autoencoding to audio by operating on spectrogram patches, using a Transformer to reconstruct masked regions and capture time-frequency patterns without relying on external modalities.

CAV-MAE [18] Combines masked autoencoding and contrastive learning in a unified audio-visual framework, using modality-specific encoders and a joint decoder to learn both fused and aligned representations from spectrogram and image patches.

FOCAL [41] Separates multimodal time-series signals into shared and private latent spaces, enforcing orthogonality and applying contrastive and temporal constraints to capture both modality-consistent and modality-exclusive features.

FreqMAE [28] Enhances masked autoencoding for multimodal IoT sensing by incorporating frequency-aware transformers, factorized fusion of shared and private features, and a weighted loss that prioritizes informative frequency bands and high-SNR samples.

PhyMask [27] Improves masked autoencoding by adaptively selecting time-frequency patches based on energy and coherence metrics, enabling efficient and informative masking tailored to physical sensing signals.

C.2 Settings for Multi-modal Multi-node Vehicle Classification Dataset

The Multi-Modality Multi-Node Vehicle Classification Dataset (M3N-VC) [34] (CC BY 4.0) comprises synchronized audio and vibration recordings of four vehicle types, along with background noise, collected from March 2023 to October 2024. Data were gathered across six distinct real-world scenes, each featuring diverse terrain types (asphalt, dirt, gravel, and concrete) and varying weather conditions (sunny, rainy, and windy).

Each scene is instrumented with a spatially distributed sensor network composed of 6 to 8 nodes. Every node includes a co-located microphone (sampled at 16 kHz) and a geophone (sampled at 200 Hz). Vehicle GPS trajectories were recorded at a rate of 1 Hz. All recordings are segmented into non-overlapping 2-second clips, resulting in a total of 21,694 samples. These clips are transformed into mel-scale spectrograms for model input. GPS coordinates are converted into meter-level spatial positions using the Local Tangent Plane approximation [1].

The dataset follows the official temporal split for training and validation (approximately 3:1). Unless otherwise noted, all models—including ours and the baselines—are pretrained on all six scenes.

We evaluate model performance on three downstream tasks:

Single-Vehicle Classification. For this task, we use scene H24 for both fine-tuning and testing. A simple linear classifier is employed as the task head, trained using standard cross-entropy loss.

Single-Vehicle Localization. This task also uses scene H24 for fine-tuning and testing. A single transformer layer is used as the task head and optimized with the mean squared error (MSE) loss.

Multi-Vehicle Joint Classification and Localization. For multi-vehicle settings, we use scene I22, which contains multiple moving vehicles. A two-layer transformer serves as the task head, trained with a DETR-style loss function [6] to handle set-based predictions.

Additionally, we conduct a **fine-tuning on unseen placement** experiment, where models are pre-trained on all scenes except H08 and H24 (which share similar placements). We then finetune and evaluate on scene H24.

C.3 Settings for Ridgecrest Seismicity Dataset

This dataset contains seismic waveform recordings from 31,452 earthquake events ($M > -0.5$) occurring between January 1, 2020, and December 31, 2024, within an 80 km radius of $(35.9^\circ, -117.6^\circ)$ in the Ridgecrest region of California. The data collection and processing procedures largely follow the methodology outlined by Si *et al.* [54].

We obtained the earthquake event catalog by querying the Southern California Seismic Network (SCSN) [5] via the Southern California Earthquake Data Center (SCEDC) [8] online catalog. The selected events include magnitudes ranging from -0.5 to 900.0 and depths between -5 km and 30,000 km. For each event, we collected three-component (East, North, Vertical) waveform data from 16 stations in the California Integrated Seismic Network, using two modalities: high-gain broadband seismometers and high-gain accelerometers. All data are sampled at 100 Hz and retrieved in miniSEED format from the SCEDC Open Data repository.

For each event, we extract a 30.72-second window from all channels as model input. During preprocessing, we detrend the waveforms and apply the Short-Time Fourier Transform (STFT) to generate spectrograms. A 2-35-Hz band-pass filter is applied to remove low-frequency noise (e.g., oceanic and atmospheric microseisms) and high-frequency instrumental or environmental noise. We convert spatial positions of each station from GPS signals to kilo-meter-level positions using Local Tangent Plane projection [1].

We split the dataset temporally: events from 2020 and 2021 are used for training, while events from 2022 to 2024 form the validation set. This results in 22,360 events in the training set and 9,092 events in the validation set.

For the downstream task of earthquake localization, we employ a two-layer transformer as the task head, optimized using the mean squared error (MSE) loss.

C.4 Settings for RealWorld-HAR Dataset

The RealWorld Human Activity Recognition (HAR) dataset [58] comprises multi-modal activity signals collected from 15 participants. The dataset captures eight common activity types: walking, sitting, lying, climbing down, running, standing, climbing up, and jumping.

Sensor data were collected from seven body-mounted nodes, located at the chest, forearm, head, shin, thigh, upper arm, and waist. For our study, we focus on three sensing modalities: acceleration, gyroscope, and magnetic field. Due to substantial data loss in the forearm sensor, we exclude that position and retain six body locations for analysis. As the dataset does not provide explicit spatial coordinates, we manually assign approximate 3D spatial positions to each sensor based on standard anatomical placement on a standing person.

All sensor signals are resampled to 50Hz and segmented into non-overlapping 4-second windows, resulting in a total of 13,351 samples. To evaluate generalization to unseen individuals, we adopt a subject-based split: data from the first 10 participants are used for training, while data from the remaining 5 participants form the validation set.

For the downstream task of human activity recognition, we use a simple linear layer as the task head, trained with standard cross-entropy loss.

D Additional Experiments Results

D.1 Evaluation on M3N-VC Dataset

Figures 3 and 4 provide additional visualizations that complement the main evaluation results. These examples offer qualitative insights into SPAR’s prediction behavior across different localization tasks.

Figure 3 presents the visualization of single-vehicle localization. The predictions generated by SPAR closely follow the ground truth vehicle trajectory throughout the scene, demonstrating strong robustness and reliable localization performance.

Figure 4 presents four representative examples from the multi-vehicle localization task, illustrating how predictions are evaluated under strict matching criteria that require both correct class identification and spatial closeness within a specified threshold. For visualization purposes, we adopt a 4-meter radius as the matching range (corresponding to the metric mAP@4m). Examples 1 and 2 (top row) show successful cases where all predicted vehicles meet both the class and spatial requirements, and are thus considered as true positives (TP). In contrast, Examples 3 and 4 (bottom row) illustrate failure cases: in Example 3, class predictions are correct, but predicted locations fall outside the 4-meter range, resulting in false positives (FP) and unmatched ground truth vehicles, which are counted as false negatives (FN); in Example 4, one vehicle is correctly localized, another is mislocalized, and an additional prediction is made for a nonexistent vehicle, yielding an extra FP. These illustrations demonstrate SPAR’s ability to produce accurate predictions under strict matching criteria.

Beyond the primary experiments presented in Section 4.1, we conduct several additional studies to further assess the robustness and generalization capability of SPAR.

The first experiment focuses on single-vehicle classification, where the objective is to distinguish among four vehicle types and a background noise class. The experimental setup mirrors that of the single-vehicle localization task. As shown in Table 5, SPAR achieves the highest accuracy and F1 score among all compared methods. The confusion matrix in Figure 5 further confirms that all five classes are well-separated, underscoring the discriminative strength of the learned embeddings.

We next evaluate SPAR’s resilience to missing data in the presence of message drops, a common challenge in real-world sensor networks. In this setting, the data points from each node have the same but independent probability of being dropped. We consider drop probabilities of 5%, 10%, and 20%, and compare SPAR’s performance against all baselines under these conditions. As reported in Table 6, SPAR consistently achieves the lowest mean squared error and distance error across all drop rates, demonstrating robust localization performance despite partial input loss.

Then, we evaluate SPAR’s ability to generalize to previously unseen sensor placements. Specifically, we pretrain all models on the full dataset except for scenes H08 and H24 (which share similar placement configurations), and then finetune and evaluate them on H24. To simulate transfer to an unseen placement, we assign each node in H24 with a structural position vector randomly selected from those learned during pretraining. As shown in Table 7, SPAR continues to outperform all baselines, even under this simple assignment strategy, demonstrating its strong generalization capability to new placements.

Finally, we conduct ablation studies on the M3N-VC dataset to evaluate the impact of each core component in SPAR. As shown in Table 8, removing geometric augmentation, excluding the spatial position reconstruction objective, or omitting spatial positional embeddings all lead to noticeable and comparable drops in performance, highlighting their complementary roles within the framework. Notably, removing the structural positional embeddings results in a more substantial degradation, emphasizing the critical importance of modeling node-specific characteristics in achieving robust and generalizable representations.

We also investigate the impact of alternative masking strategies beyond standard random masking. In Node-Drop Masking, entire nodes are fully masked prior to applying token-level random masking to the remaining nodes. In contrast, Node-Balanced Masking ensures that each node retains at least a minimum number of unmasked tokens, based on the overall mask ratio. As shown in Table 8, Node-Drop Masking leads to a decline in performance, while Node-Balanced Masking yields a slight improvement over the default strategy used in SPAR. Despite this, we adopt random masking throughout the paper to maintain conceptual simplicity and broad applicability. Finally, we explore the sensitivity of SPAR to different mask ratios by evaluating higher (0.85) and lower (0.5) values. Both of these less conventional variations result in only minor performance degradation compared to the default setting of 0.75, underscoring the robustness of our framework.

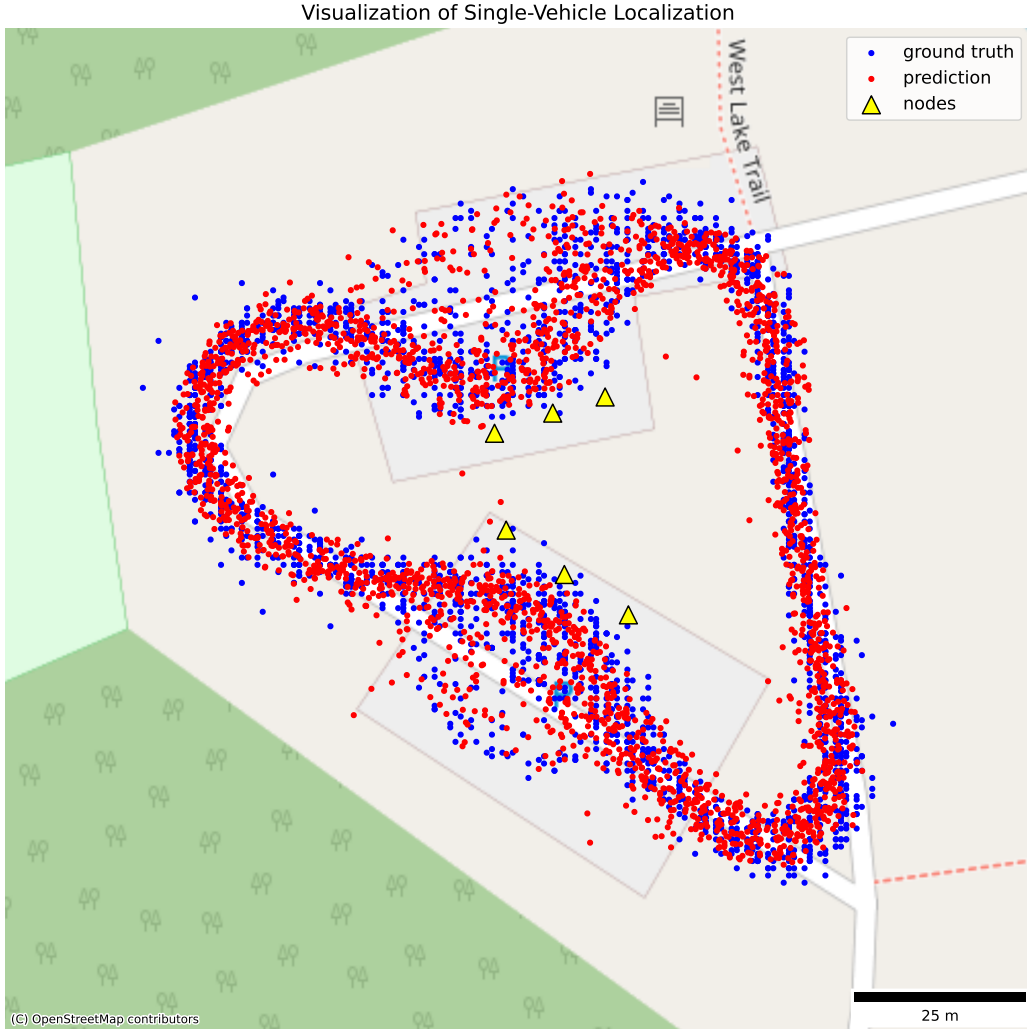


Figure 3: Visualization of single-vehicle localization. Blue dots represent ground truth vehicle location, while red dots indicate predictions by SPAR. Yellow triangles denote the spatial positions of the deployed sensor nodes. The underlying map is provided by OpenStreetMap (© contributors, ODbL).

Table 5: Comparison of the Accuracy and F1 between SPAR and baselines on M3N-VC single-vehicle classification task.

Method	M3N-VC Single-vehicle Classification	
	Accuracy (%) (\uparrow)	F1 (%) (\uparrow)
CMC	89.53 ± 7.62	89.33 ± 7.78
Cosmo	94.21 ± 0.50	94.04 ± 0.54
SimCLR	95.53 ± 0.73	95.41 ± 0.74
AudioMAE	99.06 ± 0.23	99.03 ± 0.24
CAV-MAE	98.97 ± 0.04	98.94 ± 0.04
FOCAL	93.62 ± 0.75	93.46 ± 0.76
FreqMAE	92.72 ± 0.75	92.55 ± 0.79
PhyMask	83.38 ± 2.33	82.68 ± 2.27
SPAR	99.27 ± 0.07	99.26 ± 0.07

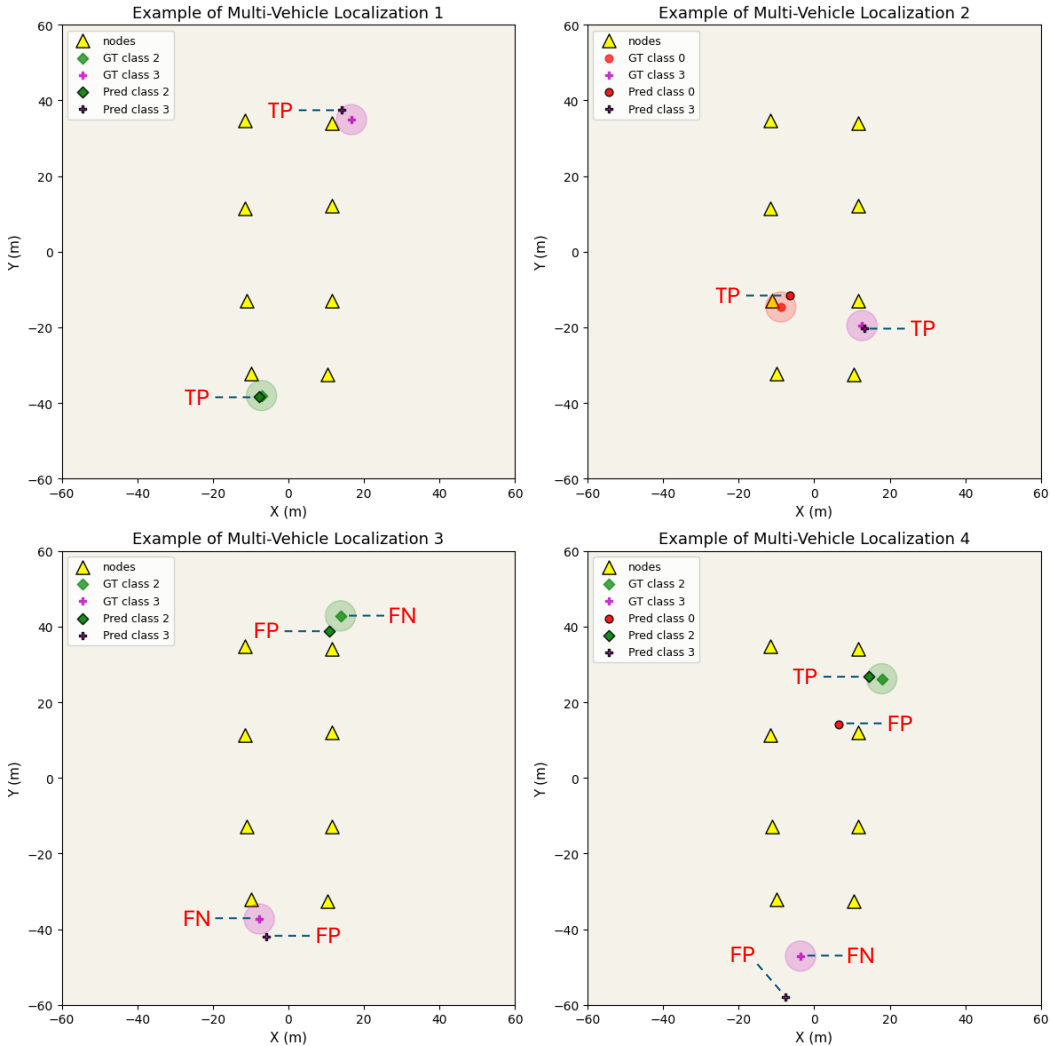


Figure 4: Representative examples from the multi-vehicle localization task. Each subplot displays the ground truth vehicle classes and locations, the predicted classes and locations, and the spatial positions of sensor nodes. A 4-meter radius is drawn around each ground truth vehicle to represent the spatial threshold used for metric mAP@4m during evaluation. Predictions that correctly match both the class and fall within this radius are labeled as true positives (TP). Predictions with incorrect class labels or those that fall outside the threshold are labeled as false positives (FP), while ground truth vehicles with no matching predictions are considered false negatives (FN). The top row shows scenarios where predictions are accurate in both class and location. The bottom row illustrates challenging cases where mismatches in class or location lead to evaluation errors.

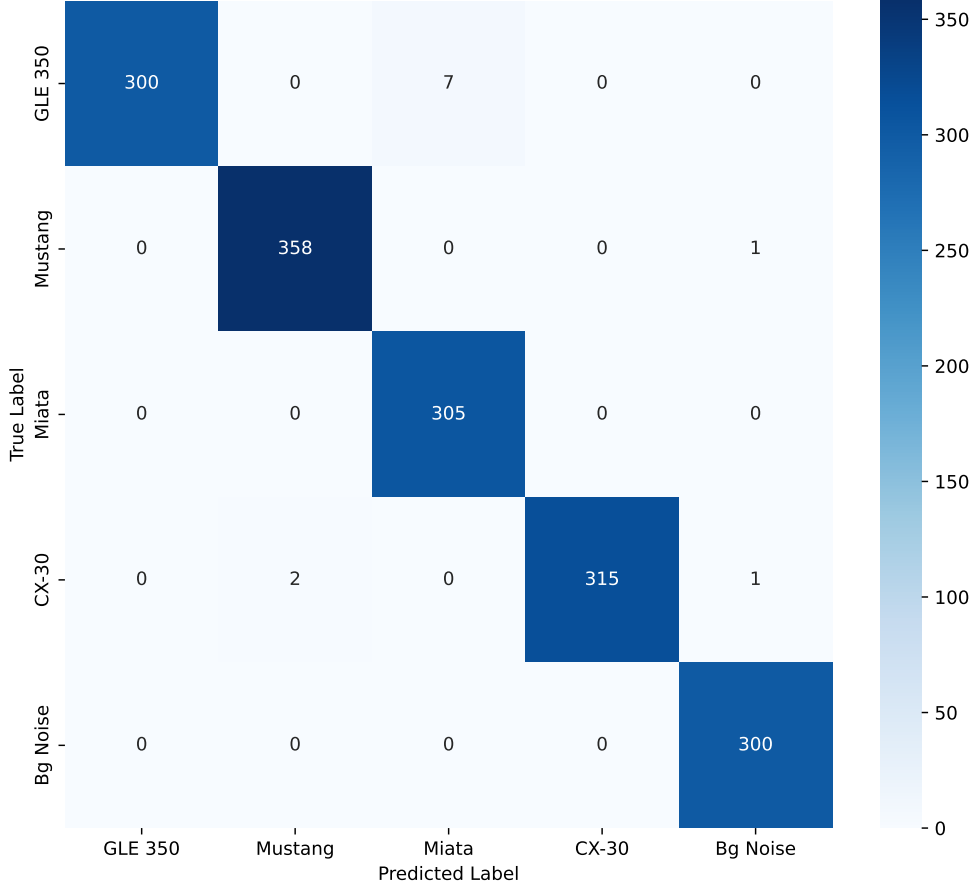


Figure 5: Confusion matrix for the single-vehicle classification task.

Table 6: Comparison of the MSE and Distance Error between SPAR and baselines on M3N-VC single-vehicle localization task, under various message drop rates.

Method	M3N-VC Single-vehicle Localization					
	Message Drop Rate 0.05		Message Drop Rate 0.1		Message Drop Rate 0.2	
	MSE (m^2) (\downarrow)	Dist. Err. (m) (\downarrow)	MSE (m^2) (\downarrow)	Dist. Err. (m) (\downarrow)	MSE (m^2) (\downarrow)	Dist. Err. (m) (\downarrow)
CMC	50.13 \pm 17.69	6.48 \pm 0.91	50.27 \pm 18.03	6.60 \pm 1.17	55.38 \pm 22.01	6.91 \pm 1.29
Cosmo	29.97 \pm 2.30	5.44 \pm 0.12	29.37 \pm 2.43	5.44 \pm 0.10	33.19 \pm 2.67	5.61 \pm 0.12
SimCLR	26.77 \pm 2.55	5.16 \pm 0.07	25.65 \pm 1.28	5.15 \pm 0.07	28.31 \pm 3.94	5.4 \pm 0.18
AudioMAE	19.29 \pm 1.42	4.91 \pm 0.17	18.25 \pm 1.23	4.77 \pm 0.10	19.03 \pm 1.14	4.77 \pm 0.05
CAV-MAE	16.28 \pm 0.17	4.68 \pm 0.03	15.85 \pm 0.81	4.57 \pm 0.10	15.98 \pm 1.67	4.44 \pm 0.12
FOCAL	26.62 \pm 1.02	5.21 \pm 0.17	27.42 \pm 2.33	5.32 \pm 0.20	33.03 \pm 2.28	5.70 \pm 0.15
FreqMAE	27.48 \pm 1.43	5.14 \pm 0.11	28.32 \pm 1.22	5.17 \pm 0.14	28.68 \pm 6.96	5.32 \pm 0.24
PhyMask	23.18 \pm 4.96	4.98 \pm 0.32	24.09 \pm 3.31	5.03 \pm 0.27	27.37 \pm 2.04	5.31 \pm 0.21
SPAR	12.65 \pm 0.61	4.09 \pm 0.11	12.48 \pm 0.68	4.07 \pm 0.02	14.56 \pm 2.47	4.27 \pm 0.07

D.2 Evaluation on Ridgecrest Seismicity Dataset

Figure 6 visualizes the earthquake localization results in the Ridgecrest region of California. SPAR produces predicted epicenters that closely align with ground truth locations, demonstrating its spatial reasoning capability.

Table 7: Comparison of the MSE and Distance Error between SPAR and baselines on M3N-VC single-vehicle localization task. SPAR and baselines are finetuned and evaluated on a placement unseen in the pretraining.

Method	M3N-VC Single-vehicle Localization (Finetuned and Evaluated on Unseen Placement)	
	MSE (m^2) (\downarrow)	Dist. Err. (m) (\downarrow)
CMC	61.78 \pm 17.68	7.23 \pm 0.78
Cosmo	63.43 \pm 12.85	7.22 \pm 0.63
SimCLR	35.82 \pm 7.57	5.92 \pm 0.39
AudioMAE	41.25 \pm 4.60	6.64 \pm 0.31
CAV-MAE	37.01 \pm 0.68	6.27 \pm 0.04
FOCAL	41.79 \pm 11.04	5.91 \pm 0.41
FreqMAE	30.65 \pm 1.14	5.51 \pm 0.19
PhyMask	34.83 \pm 8.81	5.60 \pm 0.38
SPAR	21.76 \pm 1.00	5.09 \pm 0.10

Table 8: Comparison of the MSE and Distance Error between SPAR and ablations on M3N-VC single-vehicle localization task.

Method	M3N-VC Single-vehicle Localization	
	MSE (m^2) (\downarrow)	Dist. Err. (m) (\downarrow)
SPAR	12.98 \pm 0.11	4.20 \pm 0.07
w/o Geometric Augmentation in Pretrain	15.59 \pm 0.56	4.67 \pm 0.04
w/o Reconstructing Spatial Positions	14.73 \pm 0.35	4.62 \pm 0.03
w/o Spatial Positional Embedding	15.12 \pm 0.58	4.67 \pm 0.07
w/o Structural Positional Embedding	22.55 \pm 2.98	5.08 \pm 0.13
+ Node-Drop Masking	17.71 \pm 3.17	4.82 \pm 0.33
+ Node-Balanced Masking	12.54 \pm 1.63	4.14 \pm 0.21
+ Mask Ratio 0.85	13.89 \pm 2.17	4.35 \pm 0.24
+ Mask Ratio 0.5	14.81 \pm 2.57	4.45 \pm 0.31

D.3 Evaluation on RealWorld-HAR Dataset

Figure 7 shows the confusion matrix for activity classification. The prediction patterns generally align with the conceptual separability of the activity classes.

E Discussions

While SPAR demonstrates strong performance across a wide range of IoT tasks, it has certain limitations. In particular, although the proposed learnable structural positions offer a scalable solution for capturing node-specific characteristics, there remains untapped potential in leveraging partially labeled, incomplete, or free-form metadata. For example, in human activity recognition tasks, we may have rough prior knowledge about sensor placements (e.g., “wrist-worn” or “chest-mounted”) for some nodes. Incorporating such auxiliary information could further enhance the semantic grounding of structural embeddings. In future work, we aim to develop a principled and generalizable framework for integrating this form of side information into the pretraining process—potentially with the help of large language models (LLMs) to process and interpret the free-form metadata.

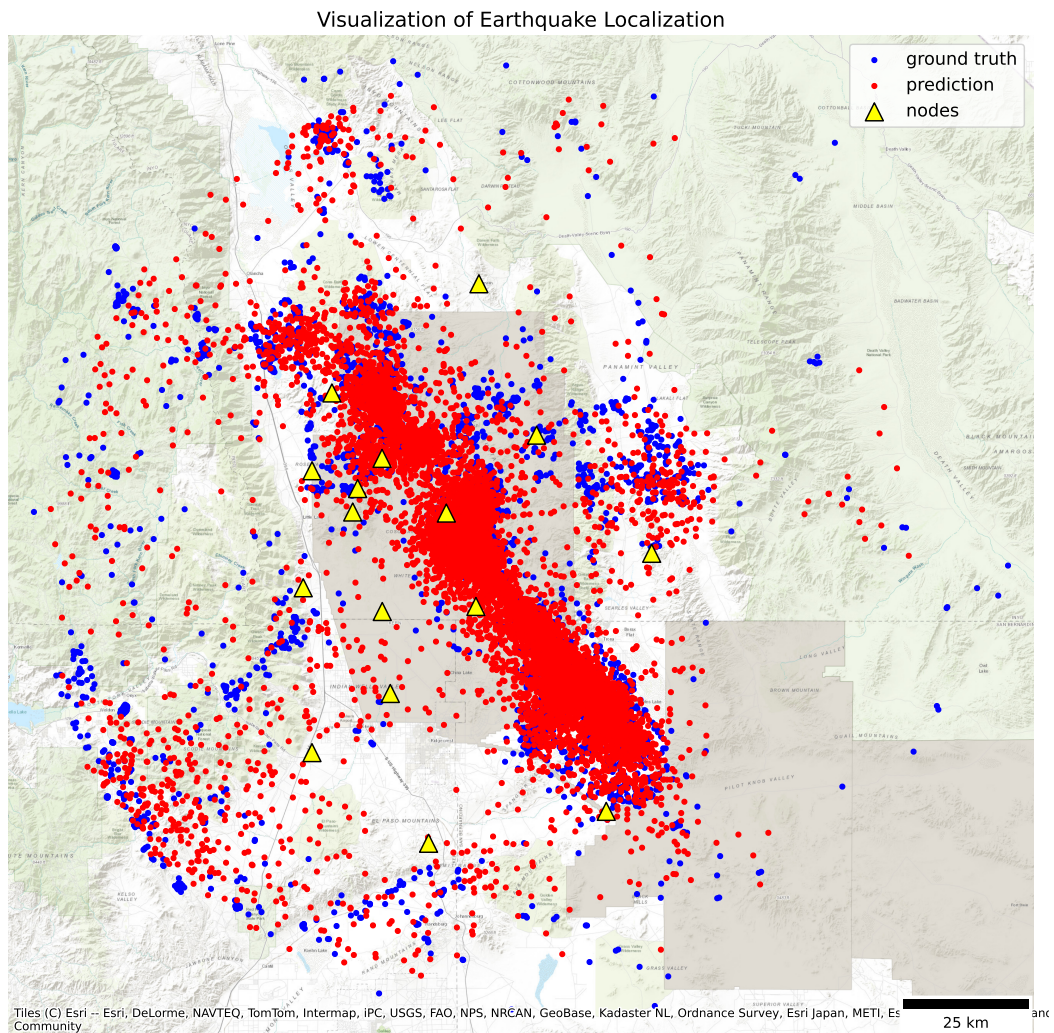


Figure 6: Earthquake localization results in the Ridgecrest region of California, overlaid on a topographic basemap. Blue dots represent ground truth epicenters, red dots indicate model predictions, and yellow triangles denote the spatial positions of stations. Background map tiles © Esri, HERE, Garmin, FAO, NOAA, USGS, EPA, NPS. Visualization generated using contextily and pyproj.

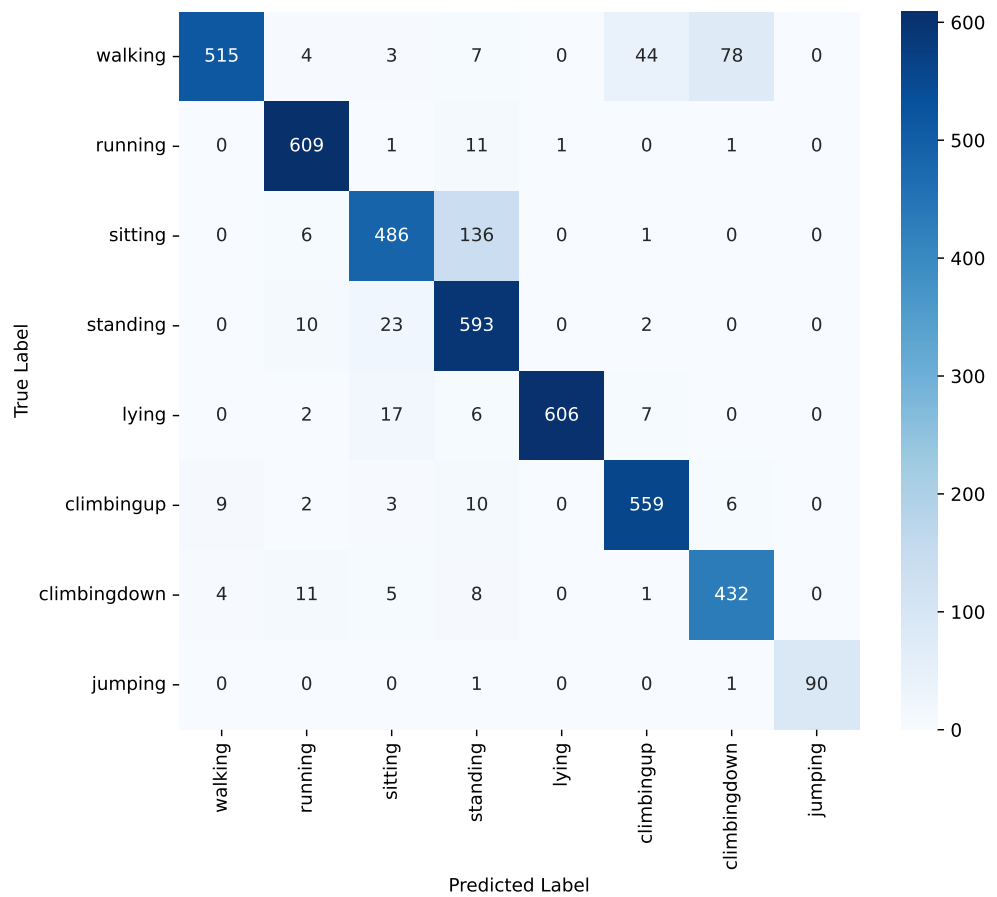


Figure 7: Confusion matrix for the activity classification task.